


Pulse modulation of synthetic jet actuators for control of separation

Thomas T. Rice , Keith Taylor , and Michael Amitay **Department of Mechanical, Aerospace, and Nuclear Engineering Rensselaer Polytechnic Institute, Troy, New York 12180, USA*

(Received 11 March 2021; accepted 13 August 2021; published 24 September 2021)

It is postulated that the pulse modulation of synthetic jet actuators at or close to the natural shedding frequency of a separated flow over an airfoil can control the shedding of vorticity, and thus the load variation exerted onto an airfoil during dynamic stall more effectively than continuous sinusoidal actuation. The forces and flowfields on and around the airfoil were used to determine the mechanism by which pulse-modulated synthetic jet actuators interact with the separated shear layer in both static and dynamic pitch conditions. Both Eulerian and Lagrangian (finite-time Lyapunov exponent) vortex identification techniques were used to identify these interactions. It was shown that pulse modulation can improve many aspects of dynamic stall control with only 35% of the power consumption compared to continuous actuation. Both shallow and deep dynamic stall cases were explored, where the hysteresis in the lift coefficient was reduced when compared to the continuously actuated case. The flowfields during deep dynamic stall showed a dramatic reduction in the size of the wake as compared to the continuously-actuated case when flow separation was present. The Lagrangian coherent structure analysis described the interaction of the synthetic jet actuators with the separated shear layer at static angles of attack. Analysis of the change in circulation through the wake of the airfoil suggested pulse modulation reduces load excursions by *reducing the maximum circulation shed from the suction side during stall inception, and increasing the circulation shed during flow reattachment*, leveling out circulation shedding while not mitigating the total circulation, or vorticity, shed. The benefits obtained by utilizing pulse modulation suggest that actuating the synthetic jets with a pulse modulation signal may have a valuable place in the use of these actuators to control dynamic stall, and a mechanism by which this is achieved is proposed.

DOI: [10.1103/PhysRevFluids.6.093902](https://doi.org/10.1103/PhysRevFluids.6.093902)

I. INTRODUCTION

Synthetic jet actuators (SJAs) have seen tremendous interest as flow control actuators due to their simple design and relative ease of installation [1–7]. Since SJAs require no pneumatic plumbing and are considered zero-net mass flux, they can provide desirable solutions to aerodynamic performance manipulations in on- and off-design conditions, and despite their low reliance on power, are able to inject relatively high momentum and vorticity into a flowfield [8]. Momentum addition and enhanced mixing is accomplished through a piezoelectric oscillator in a sealed cavity, with a thin, finite span slot of aspect ratio $O(10)$ placed at the surface. The piezoelectric disk alters the volume within the sealed cavity at a wide range of oscillating frequencies $O(100\text{ Hz})$ – $O(1\text{ kHz})$. This oscillatory change in volume, particularly at resonant frequencies, within the synthetic jet cavity (which is under the airfoil surface) creates a train of vortices that coalesce into a turbulent jet.

*Corresponding author: amitam@rpi.edu

An SJA with a finite span orifice, as used in the current study, generates a train of elliptic vortex rings, similar to those shown by [9–12], where enhanced fluid entrainment has been shown over its axisymmetric counterpart. This injection of momentum and vorticity into the flow results in a delay of boundary layer separation, which can increase lift and reduce drag on lifting surfaces, in addition to many other applications [13].

Generally, three actuation techniques can be implemented to achieve desired results: steady forcing at high amplitudes to alter the mean flow, excitation at natural (resonant-like) frequencies in the flow, taking advantage of instabilities which naturally grow [14], and excitation at frequencies that are an order of magnitude higher than the characteristic frequencies in the flow, leading to virtual shaping [15,16]. These are better understood by defining the *reduced actuation frequency*, which is the ratio of actuation frequency, f_{act} , to the shedding frequency, f_s , which is often the reciprocal of the time of flight frequency over the separated flow length, x_s , given by

$$F^+ = \frac{f_{\text{act}}}{f_s} \approx \frac{f_{\text{act}} x_s}{U_\infty}, \quad (1)$$

where U_∞ is the free-stream velocity. Thus, if $F^+ = 1$, the flow is forced at the shedding frequency. Considering a typical wind tunnel model whose chord is $c \sim O(1)$ m, SJAs are generally actuated at frequencies $O(1)$ kHz, which correspond to a reduced actuation frequency $F^+ \sim O(10)$. This actuation scheme does not excite the vortical shedding into the wake; rather, it takes advantage of the synthetic jets' ability to inject momentum, enhance mixing, and virtually reshape the flow. However, actuating near $F^+ \sim O(1)$ may yield additional benefits such as enhanced (but potentially more unsteady) lift [15,17–21].

In the current study, a combined waveform is used, where the carrier frequency is $F^+ \sim O(10)$ and is pulse modulated at a modulation frequency, f_m , on the order of the shedding frequency. This takes advantage of both the different orders of F^+ . The reduced modulation frequency of the synthetic jet is then defined such that

$$f_m^+ = \frac{f_m}{f_s} \approx \frac{f_m c}{U_\infty}, \quad (2)$$

which is analogous to the reduced actuation frequency but with the distinction that a higher frequency carrier wave is present. Here a square waveform is used to modulate the signal with a selected duty cycle (DC), which describes the portion of the period that the synthetic jets are actuated. In the current study, pulse modulation is operated at $DC = 35\%$, thus the synthetic jets were actuated only during a portion of a single pulse modulation cycle. Note that a range of duty cycles were tested (not shown here for brevity) and the results were similar once maximum jet velocity is reached. The addition of pulse modulation also has the benefit of reduced power consumption, in the current study the SJA consumes nearly one third of the power (per modulation cycle) as compared to continuous sinusoidal actuation.

A literature review yields only a modest amount of work that combines actuation parameters by forcing at both $F^+ \sim O(1)$ and $F^+ \sim O(10)$. Amitay and Glezer [21] showed that pulse-modulated synthetic jets can have significant improvement over a continuously actuated synthetic jet. Pulse modulation was also briefly investigated during dynamic stall [22], showing a 50% reduction in lift hysteresis compared to the continuously ($F^+ \sim O(10)$) actuated synthetic jet; but their work did not reveal the rich vortex interactions between the various forcing frequencies (f_m , f_{act}) and the dynamically pitching (f_p) airfoil.

A. Vortex identification

Of the many objectives of this work, one is to identify how the introduction of momentum and vorticity in this pulse-modulated manner impacts the surrounding flowfield. To do so, it is necessary to identify and describe the evolution of coherent structures in the flowfield. Many vortex identification methods used in literature are Eulerian and attempt to identify vortical structures

through the instantaneous or phase-averaged velocity field. These include vorticity, Q -criterion [23], swirling strength, λ_{ci}^2 , [24], Δ -criterion [25], and Γ_1 - and Γ_2 -criteria [26]. Vorticity as a definition of a vortex is known to fail in high shear flows, and the Q -criterion aims to remedy this. The Γ_2 -criterion uses an integrated form of normalized angular momentum about a point to define a vortex, and can be defined as

$$\Gamma_2 = \frac{1}{N} \sum_i^N \frac{\mathbf{r}_i \times (\mathbf{u} - \bar{\mathbf{u}})}{|\mathbf{r}_i| |\mathbf{u} - \bar{\mathbf{u}}|}, \quad (3)$$

which is Galilean invariant as it will detect areas of rotation as viewed in the “local” moving reference frame, whether or not that structure is evident in a visual analysis of a particular reference frame [26]. In particular scenarios, especially in high shear, Γ_2 can be a powerful method for identifying regions of flow that exhibit rotation in their own local reference frame, avoiding issues that [24] identified in their own work. Here Γ_2 is used to differentiate between regions of vortex rotation and nonvortex regions of vorticity.

Overall, *Eulerian* methods have shown some success in identifying the centers and strengths of large, coherent, vortical structures, but many times fail to describe the *interaction* between vortical structures, and are inherently not objective [27]. Lagrangian methods have been demonstrated to fill this gap. A commonly used method identifies coherent structures through the scalar finite-time Lyapunov exponent field (FTLE) [28,29]. This method integrates the trajectory of fluid particles both forwards and backwards, and finds maximum eigenvalue of the Cauchy-Green strain tensor (commonly referred to as the coefficient of expansion, σ_T) of the function that maps the particles from their original to final locations. The scalar FTLE field is then defined as $FTLE = \frac{1}{2T} \log(\sigma_T)$, where T is the integration time. Peaks in both the forward and backward integration scalar fields are isolated, and describe the highest levels of repulsion and attraction of material lines within the flow. It was also shown that this method of vortex identification is exceptional at detecting the *boundary* of coherent vortical structures, dividing between particles that are entrained into the vortex, and those that advect with the outer flow [30]. The intersection point between the positive and negative integration ridges, referred to as saddle points within the FTLE field, also give some indication to the stability of the coherent structure [31]. Although the Eulerian method gives insight to the strength of the vortex (i.e., the circulation associated with coherent rotating structures), whereas the Lagrangian method gives insight to size and overall dynamics of the coherent structure. For the current study, both methods will be leveraged to identify and analyze the interaction of various scale vortices presented during dynamic stall control.

B. Application to dynamic stall

The tracking of vortical structure, through both Eulerian and Lagrangian techniques, is necessary to understand the phenomenon of dynamic stall. A comprehensive parametric study on dynamic stall is given in [32] and is also summarized well in [33]. In his work, McCroskey characterized dynamic stall by a large vortex that forms as the flow transitions from attached to separated flow. As the effective angle of attack increases past the airfoil’s static angle of attack, the turbulent boundary layer and trailing edge separation region move upstream towards the leading edge. When flow separation ultimately moves to the leading edge, the associated vorticity within the boundary layer is concentrated in a large vortex that advects along the suction side of the airfoil. This vortex is the critical component of dynamic stall and is responsible for significant variation in the observed load. The advection of this leading edge vortex causes a temporary increase in lift, drag, and pitching moment, followed by a swift drop once this vortical structure advects away from the airfoil, resulting in a separated flowfield. This impulsive loading creates large structural oscillations, particularly if they occur at any resonant structural frequencies. As the airfoil pitches down from the maximum angle of attack, the flowfield returns to prestall conditions, with flow reattachment occurring at a lower angle of attack than in static conditions. As this generally occurs on rotating systems such as

helicopters and wind turbines, the blades are continuously rotating and these loads are repeated at every rotational cycle, adding significant fatigue to the system over time.

The current work postulates the following regarding the control of dynamic stall using synthetic jet actuators: (1) the aggressive loads experienced during dynamic stall are directly related to the vorticity generated and shed from the wind tunnel model and (2) by pulse modulating the synthetic jet actuators near the natural shedding frequency of the separated flow over the airfoil, the shedding of vorticity, and thus the loads experienced by the model could be controlled more effectively as compared to the continuously actuated case. This work dissects the control of dynamic stall using pulse-modulated SJAs by first investigating the flowfield interactions at static angles of attack in Sec. III A. Then, in Sec. III B, pulse modulation is applied to two dynamic stall cases, where the development of vortical structures and their relevance to the loads observed are analyzed.

II. EXPERIMENTAL SETUP

Wind tunnel experiments were conducted at RPI's open return wind tunnel at the Center for Flow Physics and Control. The wind tunnel has a $0.8 \text{ m} \times 0.8 \text{ m} \times 5 \text{ m}$ test section, and was rated to have a free-stream turbulence intensity less than 0.2% at a maximum speed of 50 m/s. The experimental data presented here were obtained at a chord-based Reynolds number of $\text{Re}_c = 375\,000$, where $\text{Re}_c = U_\infty c / \nu$, corresponding to a free-stream velocity $U_\infty = 20 \text{ m/s}$. In order to ensure the boundary layer over the model was turbulent, a small boundary layer trip consisting of double-sided tape and no. 36 grit aluminium oxide was placed at the 5% and 10% chordwise locations, on the suction and pressure sides, respectively.

The wind tunnel model had span $b = 0.46 \text{ m}$ and chord $c = 0.28 \text{ m}$ and was connected on both ends to side walls. The walls were placed 1 mm from the tip to prevent the tip vortex from forming while allowing changes in the angle of attack. The model's surface was fabricated with additive manufacturing, specifically utilizing stereo-lithography with a resolution of 0.125 mm. The model was rigidly connected to a DC motor, which allowed for changes in angle of attack both in static and dynamic conditions. The angle of attack was monitored by an external encoder with an uncertainty of $\pm 0.18^\circ$.

Three critical pitch parameters have a large effect on dynamic stall: mean pitch angle of attack, $\bar{\alpha}$, pitching amplitude, α_A , and pitch frequency, f_p . The sum of mean pitch angle of attack and the pitch amplitude corresponds to the maximum angle of attack, and the difference to the minimum angle of attack. Thus, these parameters directly impact how deep into stall the airfoil pitches and the rate of pitching in stall. The pitch frequency is represented nondimensionally by the reduced pitch frequency, given by

$$k_f = \frac{\pi f_p c}{U_\infty}. \quad (4)$$

For the dynamic pitch cases presented in the current study, pitch parameters were chosen such that the model pitched past its stall angle at a reduced frequency $k_f = 0.025$. For the dynamic pitch experiments, the mean angle of attack, $\bar{\alpha}$, was chosen to be the angle near the maximum lift coefficient. Two pitching amplitude, α_A , were tested, which allowed the model to be pitched into and out of stall in shallow and deep conditions, where pitching amplitudes of 3° and 5° represent shallow and deep dynamic stall, respectively. The dynamic motion was prescribed using a National Instruments PCI-7342 motion controller, which was given a sinusoidal command for the angle of attack, represented as

$$\alpha = \bar{\alpha} + \alpha_A \sin(2\pi f_p t). \quad (5)$$

Figure 1 presents a schematic of the wind tunnel model. Nine evenly spaced SJAs were installed on the model. The SJAs had an orifice size of $12 \text{ mm} \times 1 \text{ mm}$ and were placed at either $x/c = 0.15$ or 0.35 , with four orifice lengths between the centerline of each SJA. These actuator locations represent implementation near the leading edge and upstream of the location of maximum thickness,

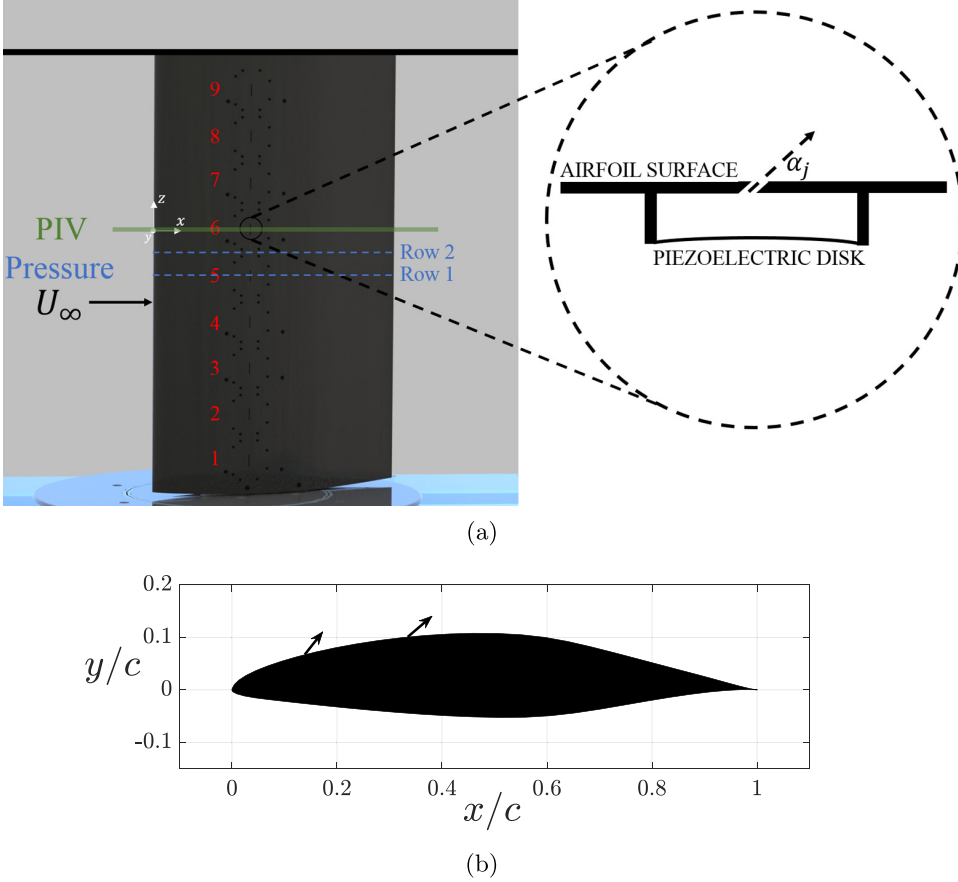


FIG. 1. S817 wind tunnel model description. (a) Diagram of wind tunnel model, including the synthetic jets, numbered from bottom to top in increasing order, representative planes of data collection, with synthetic jet diagram. (b) S817 airfoil section with synthetic jet locations and incidence. Note that only one array of synthetic jet location was actuated at a time.

respectively, of the S817 airfoil previously used for field testing of SJAs on a utility scale wind turbine [34]. The synthetic jet orifices were angled at 45° to the surface of the airfoil, facing downstream, as shown in Fig. 1(b), which allows for an effective combination of momentum and vorticity added into the flow [35]. The diaphragms used to drive the synthetic jets were a custom design produced by MIDE Technology, and incorporate two piezoelectric wafers in a single diaphragm. The velocity of each synthetic jet was determined by placing a hotwire at the midspan and midwidth orifice position. All synthetic jets were driven in phase, and at the same peak velocity. The synthetic jets are characterized by their blowing ratio, C_b , and by the momentum coefficient, C_μ , where

$$C_b = \bar{u}_{sj}/U_\infty, \quad (6)$$

$$C_\mu = \frac{n\bar{I}_j}{\frac{1}{2}\rho_\infty U_\infty^2 S}, \quad (7)$$

where \bar{u}_{sj} is the average jet velocity during the blowing portion of the cycle, n is the number of active synthetic jets, S is the airfoil's planform area, and \bar{I}_j is the time-averaged synthetic jet momentum

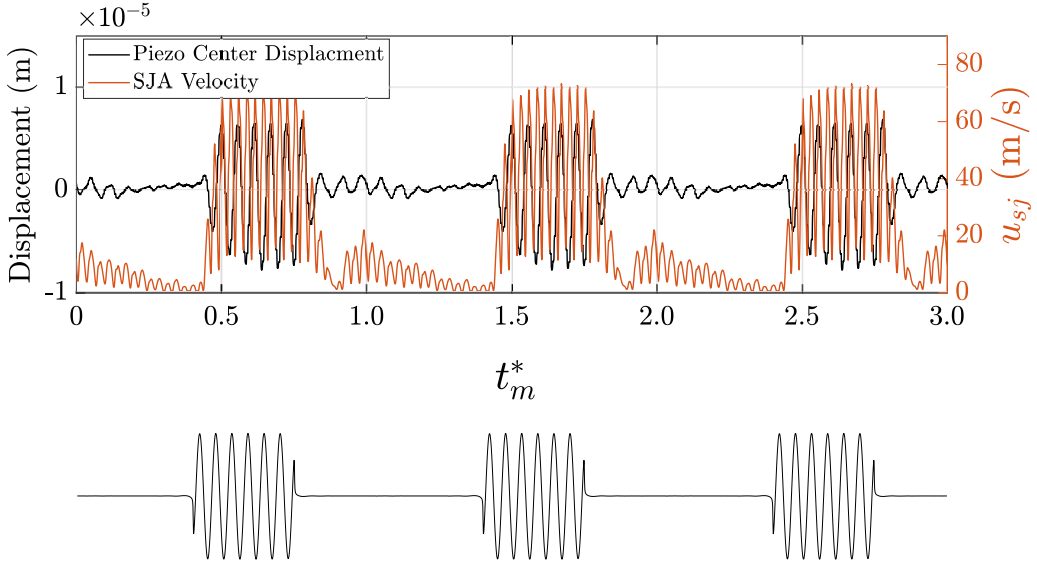


FIG. 2. SJA response to pulse modulation signal driven at $f_{\text{act}} = 1800$ Hz, $f_m = 100$ Hz and $DC = 35\%$, including the disk centerline peak displacement and the jet velocity, with the input driving signal shown on the bottom.

during outstroke. \bar{I}_j can be written as

$$\bar{I}_j = \frac{1}{\tau} \rho_{sj} A_{sj} \int_0^{\tau} u_{sj}^2(t) dt, \quad (8)$$

where A_{sj} is the synthetic jet orifice area and τ is the half of the actuation period time. The synthetic jets were actuated at a momentum coefficient $C_\mu = 0.012$ and blowing ratio $C_b = 1.2$, corresponding to a peak jet velocity of 75 m/s, and were actuated near the resonant frequency of the piezoelectric disk ($f_{\text{act}} = 1800$ Hz), corresponding to a reduced actuation frequency $F^+ = 25$. The values chosen have been shown to be effective in penetrating the boundary layer [35] and at controlling dynamic stall [22,36].

When pulse modulation was employed, the synthetic jets were modulated at $f_m = 100$ Hz, which correspond to $f_m^+ \sim 1$. The shedding frequency was found by two omni-directional Sonion 8000-series microphones embedded in the airfoil surface at $x/c = 0.55$ and 0.75 and were sampled at 10 kHz for 20 s. A broad peak centered on $f = 100$ Hz was observed at an angle of attack $\alpha = 20^\circ$, which was used for the static angle of attack tests. The response of the diaphragm, as well as the jet exit velocity, to a pulse modulation signal was measured to ensure that the desired frequencies and velocity were produced. This was conducted with hotwire testing in conjunction with an LK-G80 laser displacement sensor, with an uncertainty of $\pm 0.2 \mu\text{m}$, sampled at 20 kHz, and averaged over 10 modulation cycles to obtain the diaphragm's displacement response. Figure 2 presents the phase-average diaphragm displacement and jet exit velocity in response to a pulse modulation input signal, where the SJA is driven at a carrier frequency $f_{\text{act}} = 1800$ Hz, a modulation frequency $f_m = 100$ Hz, and a duty cycle $DC = 35\%$. Normalized time, t_m^* , is presented, which is normalized by the period of the pulse modulation cycle (in this case, 10 ms). The SJA is observed to reach a peak velocity in four cycles (noting that the hotwire voltage shows two peaks per cycle due to rectification of the signal), and operates at the peak velocity amplitude for three cycles until the input voltage is set to zero, and the velocity decays quickly. A resonant response, where $u_{sj} < 20$ m/s, is observed during the off portion of the cycle, but is hypothesized to have a minimal effect on the flow.

An six-component ATI Delta load cell was used to collect pitching moment coefficient data, which were averaged over 60 s at a sampling frequency of 5.7 kHz. For the load range taken in this study, the calibration report obtained from ATI indicated an error of $< 0.25\%$, corresponding to $\pm 0.15\text{N}\cdot\text{m}$. Data collected from the load cell data were low-pass filtered using a digital fourth-order Butterworth filter with a cutoff frequency of 600 Hz to remove electrical noise associated with the actuation of the synthetic jets at 1800 Hz.

Surface pressure measurements were obtained using three Scanivalve model DSA3217 pressure scanners, which have an uncertainty of 0.12% of their max value of 1 psid, and were sampled at 125 Hz for 10 s for static cases, and 60 s for dynamic cases. Data from two rows of pressure taps (in-line and in between SJAs) were averaged near the midspan of the wind tunnel model, and are also shown in Fig. 1(a). Integration of the pressure distribution was used to determine all sectional lift and pressure drag forces presented, and was conducted with linear interpolation between measurement points. Due to the thin trailing edge, the closest pressure measurement to the trailing edge was at 95% chord on the suction side, and 90% chord on the pressure side. The uncertainty associated with the lift integration was determined using the uncertainty of the pressure and temperature measurements. Uncertainty of the pressure coefficient, C_p , was determined to be ± 0.03 , corresponding to an uncertainty of integrated force coefficient of ± 0.01 . However, there are certain parameters not included in this analysis that may also affect aerodynamic coefficient uncertainty, such as the extrapolation of pressure coefficient to the trailing edge, the point-wise nature of pressure measurements (and the subsequent linear interpolation), and the effect of angle of attack uncertainty on the pressure coefficient distribution. Thus, the authors recognize additional uncertainties may exist in the lift coefficient; however, as the focus of the current study is the relative change in lift coefficient, and many of the errors listed above are assumed to be biased, the effect of error on the *trends* observed is assumed to be minimal.

Quantitative flowfield measurements were obtained using stereoscopic particle image velocimetry (SPIV) at the jet 6 location as shown in Fig. 1(a). The SPIV system utilized a dual pulsed Nd:YAG laser with a maximum output of 120 mJ/pulse and two 2 megapixel (1608×1208 px) LaVision Imager LX cameras, placed $\sim 45^\circ$ apart from each other. A Scheimpflug adaptor was placed between each camera and a 35 mm lens in order to account for the angle between the camera lens and the image plane. The flow was seeded using a theatrical fog machine, which created water-based particles of size $\sim O(1 \mu\text{m})$. Images were taken both in the time- and phase-averaged sense. Images were phase locked to the synthetic jet input voltage at various phases along the pulse modulation cycle during static angles of attack. During dynamic pitching, images were phase locked to airfoil pitching motion. Coordinates for this experiment are such that +X is downstream, and +Y is transverse towards the airfoil suction side.

Five hundred image pairs were acquired for all static angle of attack data sets, and the flowfield associated with *dynamic stall* used 250 image pairs, phase locked to the motion of the airfoil. These values were chosen to ensure statistical convergence of the mean flow and RMS while minimizing acquisition time and SJAs wear. Twenty-four phases were captured per cycle during dynamic pitch, and 40 phases during the pulse modulation. The velocity components were computed using three-step stereo cross correlation with 50% overlap between interrogation domains, where the final correlation windows were 16×16 px. Utilizing the uncertainty analysis provided in DaVis 10 (outlined in [37]), the uncertainty in the velocity field varied from $\pm 0.005U_\infty$ in the free stream to $\pm 0.10U_\infty$ in the separated shear layer. The Lagrangian coherent analysis was performed on the midspan plane PIV data (which exhibited low spanwise flow velocity), utilizing LCS MATLAB Kit v2.3 [38] and was integrated for three pulse modulation cycles, approximately a time of flight of a vortical structure over the airfoil.

An investigation into the variation of observed circulation associated with rotating structures was devised, and the process is outlined as follows: the Γ_2 criterion criterion was selected for the identification of a rotating structure in a given instantaneous flowfield. Then vorticity fields were computed for all instantaneous fields. Γ_2 was then computed for the same vector field, and all values above $2/\pi$ and less than $(-2/\pi)$ were isolated, which represent regions associated with

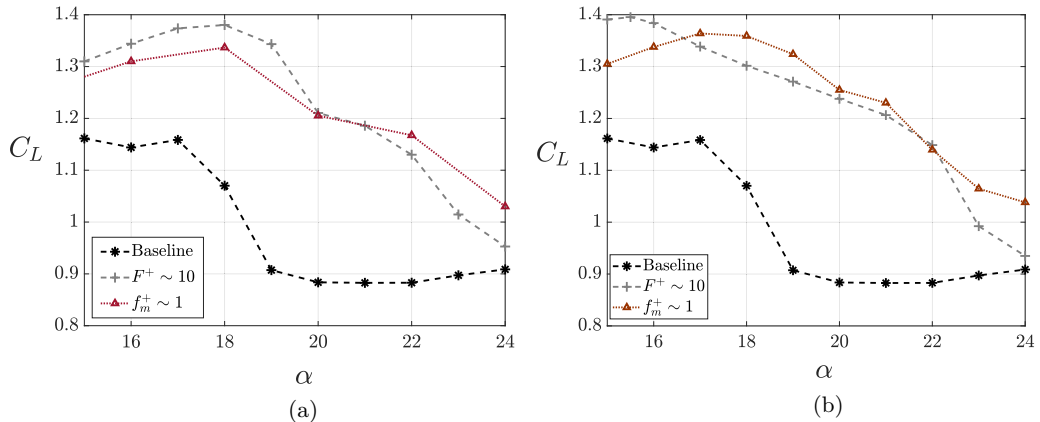


FIG. 3. Variation of the lift coefficient with angle of attack near stall when either pulse modulation waveform (at $f_m = 100$ Hz and $DC = 35\%$) or continuous sinusoidal waveform are implemented, and are compared to the baseline case. The SJAs are placed at (a) $x/c = 0.15$ and (b) $x/c = 0.35$.

structure rotation [26]. Γ_2 was selected over the Q -criterion as the metric by which to judge vortices since Γ_2 has the advantage of spatially filtering small structures, is Galilean invariant, and is more effective in regions of high shear when compared to the Q -criterion. In order to determine the circulation associated with rotating structures, the map created by Γ_2 was used to choose the locations for area integration of circulation. The purpose of this method is to compute the contribution to circulation from integrated vorticity of the rotating structures, and split this off from the contribution to circulation from vorticity in the boundary layer and shear layer not associated with rotating structures (or at the very least leave out particularly small structures from this integration). Additionally, using Γ_2 as the criterion to choose regions of rotating structure, the sign of Γ_2 may be used to isolate regions where a structure is rotating positively or negatively, even if there is local “noise” in the vorticity.

This process was conducted for three variations: to isolate the vorticity associated with positive rotation, to isolate the vorticity associated with negative rotation, and to isolate regions with vorticity not associated with rotating structures. By calculating the mean and the standard deviation of the circulation during dynamic stall, it is possible to plot bands of the change in circulation isolated to positively rotating structures, negatively rotating structures, and “nonrotational” vorticity (such as vorticity typically observed in shear layers or in boundary layers). An integration region of four levels was selected, the N as indicated in Eq. (3), as the spacing in x and y of the SPIV data (1.68 mm per vector) would suggest this region to be large enough to filter out small structures observed in the free stream which arise due to the error in the SPIV measurements in this region.

III. RESULTS

The results presented are divided into two sub-sections, where first the interaction of the synthetic jets with the flowfield at static angles of attack is discussed in Sec. III A. Then, in Sec. III B, the effect of the SJAs during dynamic stall is presented.

A. Static angle of attack results

The effect of the SJAs on the lift coefficient when driven with a pulse-modulated waveform compared to traditional continuous sinusoidal waveform is shown in Figs. 3(a) and 3(b) for SJAs placed at $x/c = 0.15$ and $x/c = 0.35$, respectively. At high angles of attack, the pulse-modulated SJAs provide more lift enhancement as compared to the continuous actuation, and past the intersection

point of the lift coefficient curves for each actuation technique ($\alpha = 20^\circ$ for the $x/c = 0.15$ case and $\alpha = 16.5^\circ$ for the $x/c = 0.35$ case), as α is increased, the pulse-modulated technique enhances the lift coefficient. Lift enhancement as high as 10% compared to the continuously actuated technique is observed. It is postulated that pulse modulation is more effective in increasing the lift coefficient as compared to the continuously actuated case when $\alpha > \alpha_{C_{L,\max}}$ (for $\alpha_{C_{L,\max}}$ of the continuously actuated case). This suggests that pulse modulation is more effective than continuous actuation when the flow remains separated. This is expected as the existence of a shear layer is required to be able to excite the frequencies associated with it. This observation is specifically relevant to the current work as its aim is to reduce the unsteady loads during deep dynamic stall, when the continuously actuated SJAs are unable to keep the flow attached throughout the dynamic pitch cycle. Contours of time-average total velocity are presented in Fig. 4 with the separation line to observe the effect of the driving waveform on the flowfield. Here the airfoil is placed at $\alpha = 20^\circ$, and the pulse modulation parameters remain at $f_m = 100$ Hz and $DC = 35\%$. The baseline case is presented in Fig. 4(a), followed by the continuously actuated cases when the SJAs were at $x/c = 0.15$ 0.35 [Figs. 4(b) and 4(c), respectively], and the corresponding pulse-modulated cases [Figs. 4(d) and 4(e), respectively]. All actuated cases reduce the cross-stream extent of the recirculation region and the size of the wake, with a higher velocity near the leading edge, thereby increasing the suction magnitude and producing more lift as shown in Fig. 3. More importantly, a comparison between the continuously actuated cases [Figs. 4(b) and 4(c)] and the pulse-modulated cases [Figs. 4(d) and 4(e)] indicates a further reduction of the extent of the separated region compared to the corresponding continuously actuated cases. It is clear that when the flow is fully separated for the continuously actuated case, such as at $\alpha = 20^\circ$, pulse modulation provides a greater reduction to wake size as compared to the continuously actuated case.

Next, the phase-averaged fields for the pulse-modulated case (SJA location $x/c = 0.15$) is presented in Figs. 5 and 6 using the Q -criterion as a vortex identification method (where $5 < Q^* < 50$). Figure 5 describes the phase-averaged pulse modulation case at $t_m^* = 0.6$ (t_m^* is the nondimensional modulation time, $t_m^* = t f_m$). The actuation timescale remains as was presented in Fig. 2, where the SJAs are active from $0.4 < t_m^* < 0.6$. The circle near the SJA orifice describes the main vortical structure that the SJA is emitting into, and the two red arrows highlight the smaller vortical structures expelled from the SJA at $f_{\text{act}} = 1800$ Hz, which amalgamate into the larger vortical structure. The circle near $x/c = 0.7$ shows the remnants of the vortical structure shed in the preceding actuation cycle (of the pulse modulation frequency). This indicates that when pulse modulated over a separated flowfield, the SJAs have the ability to shed vortical structures as described by the Q -criterion.

Next, Fig. 6 shows the phase-averaged Q -criterion over multiple time periods, used to visualize the shedding of vortices during a full pulse modulation cycle. Images are presented at $0.1 t_m^*$ intervals. Figure 6(a) shows the flowfield at $t_m^* = 0.7$ (see Fig. 2 for reference), where the aforementioned leading edge vortex is observed to gain strength and coherence (defined by the darkening and amalgamation of positive Q levels) from $t_m^* = 0.7$ to 0.8 [Figs. 6(a) and 6(b), respectively] as the SJA is still actuated. At $t_m^* = 0.9$ [Fig. 6(c)] the SJA is off, and the large vortical structure begins to shed and advect in the downstream direction, where there is local recirculation region, as seen by the average in-plane streamlines. In Fig. 6(d) ($t_m^* = 1$), the vortex is observed to advect further downstream, and is located at $x/c = 0.35$. Three distinct vortical structures are observed: one in the immediate vicinity of the leading edge (and upstream of the SJA orifice), the aforementioned vortex that is being shed at the pulse modulation frequency, and the trailing edge recirculation region. These structures are highlighted by the arrows in Fig. 6(d). It should be noted that the trailing edge structure is *not* identified by the Q -criterion nor coherently observed in a respective instantaneous image, and will thus be referred to as a recirculation region (instead of a coherent vortex). Next, Figs. 6(e)–6(i) describe the start of the next cycle (as defined by Fig. 2), and represent $0.1 < t_m^* < 0.5$, where the shed vortical structure is observed to continue to advect downstream and dissipate as it loses strength and coherence, finally combining with the trailing edge recirculation region. Ultimately, these are a direct observation of a vortex structure being *created*, and subsequently *shed*, by the

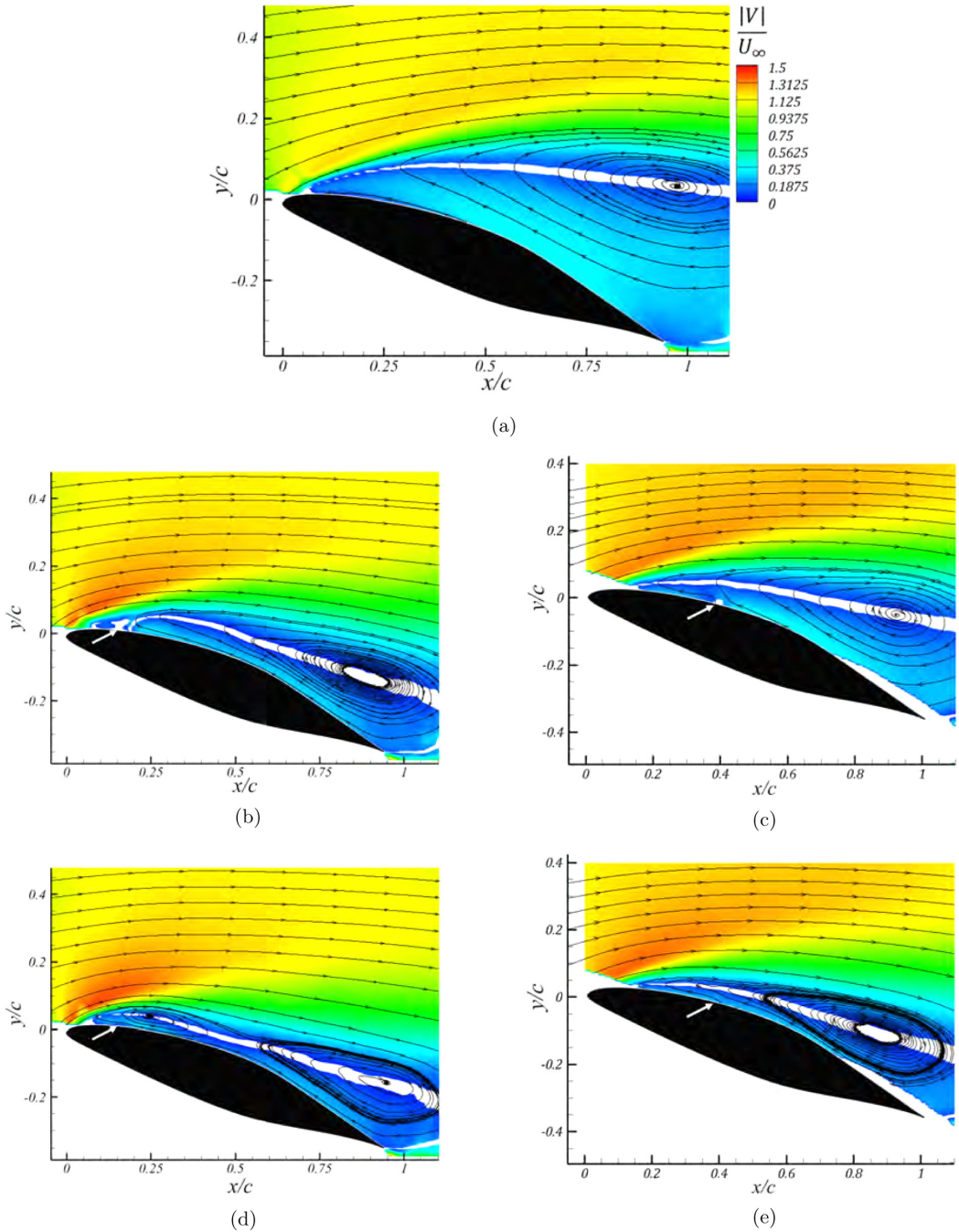


FIG. 4. Contours of time-averaged normalized total velocity with separation contour ($|u/V| < .05$) at $\alpha = 20^\circ$ for (a) baseline, (b, c) continuous sinusoidal actuation at $F^+ \sim O(10)$, and (d, e) pulse-modulated actuation with $f_m^+ \sim O(1)$. SJAs at (b, d) $x/c = 0.15$ and (c, e) SJAs $x/c = 0.35$ (marked by the white arrows).

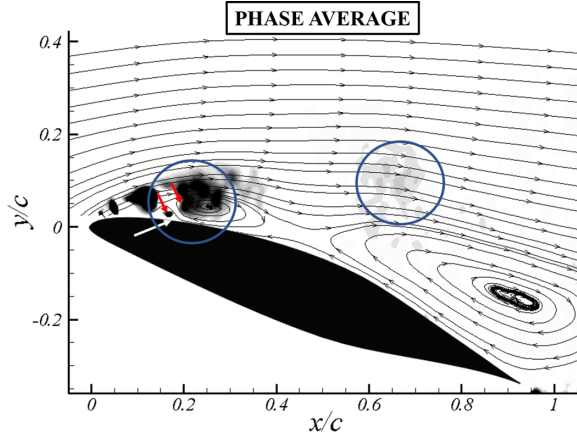


FIG. 5. Contours of Q^* ($5 < Q^* < 50$) for a phase-averaged pulse-modulated flowfield at $t_m^* = 0.6$. SJAs at $x/c = 0.15$, $f_m^+ \sim O(1)$, and $\alpha = 20^\circ$.

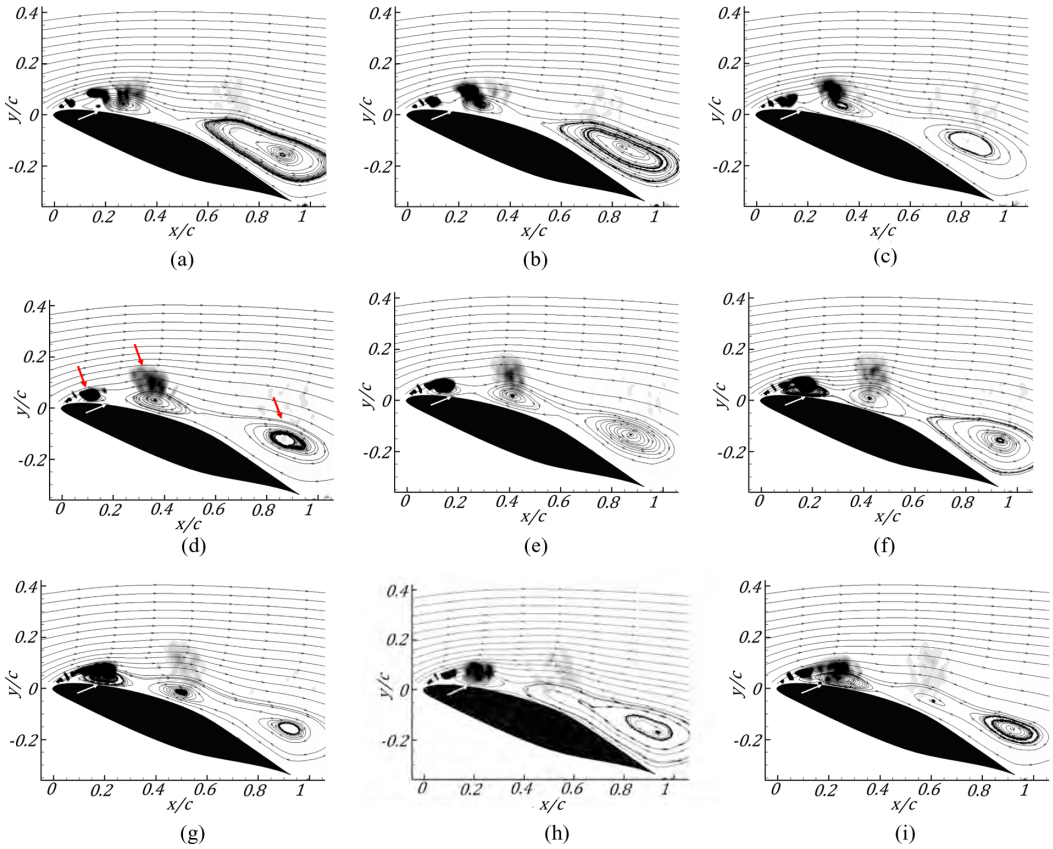


FIG. 6. Contours of phase-averaged Q^* ($5 < Q^* < 50$) at $\alpha = 20^\circ$ and $f_m^+ \sim O(1)$ actuated at $x/c = 0.15$, for (a) $t_m^* = 0.7$, (b) $t_m^* = 0.8$, (c) $t_m^* = 0.9$, (d) $t_m^* = 1.0$, (e) $t_m^* = 0.1$, (f) $t_m^* = 0.2$, (g) $t_m^* = 0.3$, (h), $t_m^* = 0.4$, (i) $t_m^* = 0.5$.

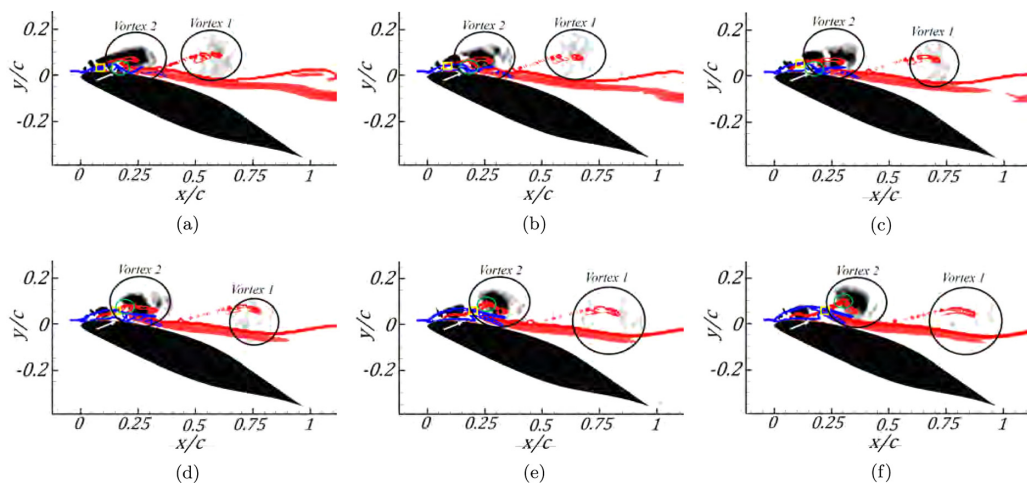


FIG. 7. Contours of phase-averaged Q^* ($5 < Q^* < 50$), in conjunction with FTLE analysis, at $\alpha = 20^\circ$. Pulse modulation with $f_m^+ \sim O(1)$, SJAs at $x/c = 0.35$, for normalized times of (a) $t_m^* = 0.5$, (b) $t_m^* = 0.6$, (c) $t_m^* = 0.7$, (d) $t_m^* = 0.8$, (e) $t_m^* = 0.9$, (f) $t_m^* = 1.0$.

pulsed actuation of the SJAs. However, as has been suggested in Sec. I, little information regarding the interaction of coherent structures is revealed through the Q -criterion; thus, an analysis, using the Lagrangian coherent structures, is present next.

Figure 7 shows the positive (blue), and negative (red) FTLE ridges in the phase-locked flowfields at select times during the pulse modulation cycle. In Fig. 7 multiple indicators are superimposed on the flowfields to help describe the multiple occurring events. Similar to Fig. 6, two vortices are observed in each frame: one currently being shed (from the midspan downstream), and one near the leading edge, which is actively forming. These are labeled vortex 1 and 2, respectively. Next, disturbances in the FTLE ridges by the small-scale, high-frequency synthetic jet vortices are highlighted by the green circle, and the FTLE saddle point of the leading edge vortex is shown by the yellow square. As the saddle point is quite close to the airfoil surface, they are more visible in Fig. 8, which provides a zoomed-in version of the same series of images. The series of images presented in Fig. 8 describe the shedding process for $0.5 < t^* < 1.0$, defined by the lift-off of this saddle point from the surface.

In Figs. 7(a) and 8(a), the saddle is still attached to the airfoil surface and the concentration of Q^* is still connected to the leading edge; thus, vortex 2 can be stated to have not yet been shed. The nFTLE ridges (red) show three wavelike structures, each associated with a vortical structure. Within the green circle, Q -concentrations, although difficult to see, are being emitted from the orifice and are disturbing the local FTLE ridges. At $t_m^* = 0.6$ [Figs. 7(b) and 8(b)], the saddle point begins to move away from the airfoil surface, suggesting that the shedding process has begun. As time progresses [Figs. 7(c) and 8(c)], the saddle point has moved away from the airfoil surface, and the concentration of Q^* begins to detach from the leading edge. At $t_m^* = 0.8$ [Figs. 7(d) and 8(d)], the first indication of the interaction between the main vortical structure and the small-scale synthetic jet vortical structures is observed, and highlighted by the green circle, which describes a bumplike feature on the nFTLE ridge associated with vortex 2. This is further evident in Figs. 7(e) and 8(e), where the bump in the nFTLE ridge is more prominent, and is observed to rotate around the leading edge vortex, in the clockwise direction, and the saddle point continues to advect downstream. Finally, at $t_m^* = 1.0$ [Figs. 7(f) and 8(f)], the saddle point and the Q^* concentration have been shed, and the bumplike feature is once again observed to further rotate in the clockwise direction. This suggests that the SJA pulses excite the vortex *upstream* of where it is formed, and that the small-scale SJA vortices amalgamate around the outside of the large scale leading edge vortex that is being shed.

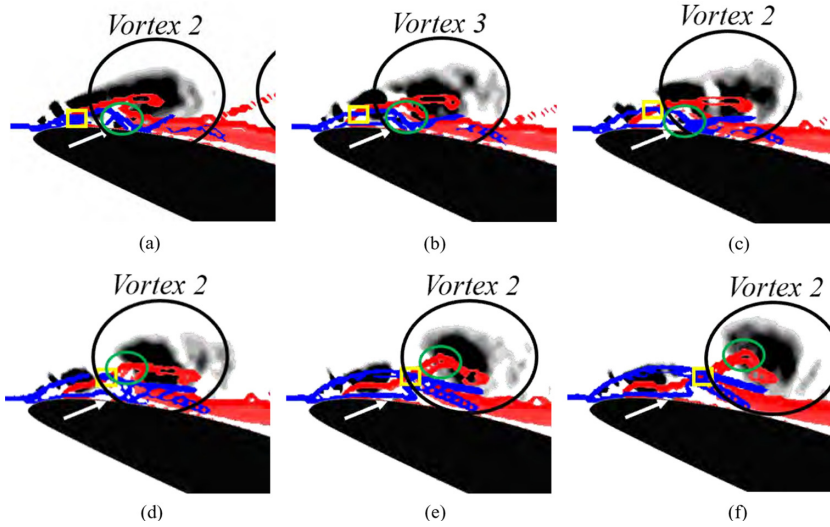


FIG. 8. Zoomed-in contours of phase-averaged Q ($5 < Q^* < 50$), in conjunction with FTLE analysis, at $\alpha = 20^\circ$. Pulse modulation with $f_m^+ \sim O(1)$, SJAs at $x/c = 0.15$, for normalized times of (a) $t_m^* = 0.5$, (b) $t_m^* = 0.6$, (c) $t_m^* = 0.7$, (d) $t_m^* = 0.8$, (e) $t_m^* = 0.9$, (f) $t_m^* = 1.0$.

Figure 9 shows similar FTLE contours to the $x/c = 0.15$ SJA location case but includes more time steps to better illustrate the complex flow interactions. Flowfields are shown from $0.5 < t_m^* < 1.3$. The flowfield for $t_m^* = 0.5$ is shown first, in Fig. 9(a), as it is the first instance where disturbances from the SJA can be observed near the actuator orifice, as suggested by the small concentration of Q . Here the saddle point for vortex 2 is still attached to the airfoil surface, and the Q -concentration associated with vortex 1 has already been shed and is advected downstream. Next, in Fig. 9(b) the SJA continues to actuate, where in Fig. 9(c) the effect of the actuation is observed in the dividing separation line between the two shed vortices. In fact, it is observed that the small-scale, high-frequency vortex pairs from the SJA push away, and add an undulation to shear layer trajectory. This is indicated by the outward facing black arrow near the actuator orifice. At $t_m^* = 0.8$ [Fig. 9(d)], an nFTLE ridge is observed between the two counter-rotating synthetic jet vortices, as shown in the green circle. In addition, the saddle point associated with vortex 2 is observed to advect away from the airfoil surface, indicating that the shedding process has begun.

As time advances from $0.9 < t_m^* < 1.3$ [Figs. 9(e)–9(i)], an important observation is made. As the saddle point associated with the leading edge vortex advects downstream, the nFTLE ridge disturbance by the synthetic jet (in the green circle) is observed to advect *upstream*. This is an important observation, as it suggests a different mechanism than when the SJAs are actuated closer to the leading edge. In fact, if the reader diverts their attention back to Fig. 9(a), and continues to follow the disturbance by the synthetic jet, it can be observed that ultimately, it amalgamates with the *next* leading edge vortex, and not with the one that sheds with the actuation (unlike when actuating from $x/c = 0.15$).

To summarize, when actuating at $x/c = 0.15$, the small-scale vortex pairs coalesce around the outside of the forming leading edge vortex. However, when the SJAs, located at $x/c = 0.35$, are actuated, their vortex pairs move *upstream* with the reversed, recirculating flow, as the leading edge vortex is shed, and amalgamates into the *next* vortex that is to be formed. These are two different mechanisms that seem to have the same impact on the flowfield.

An analysis of the circulation shed during the SJAs actuation cycle (utilizing pulse modulation) is presented next to explore their effectiveness on the shed circulation. The change in circulation was calculated along the suction side of the wake by summing the negative vorticity (in time), along

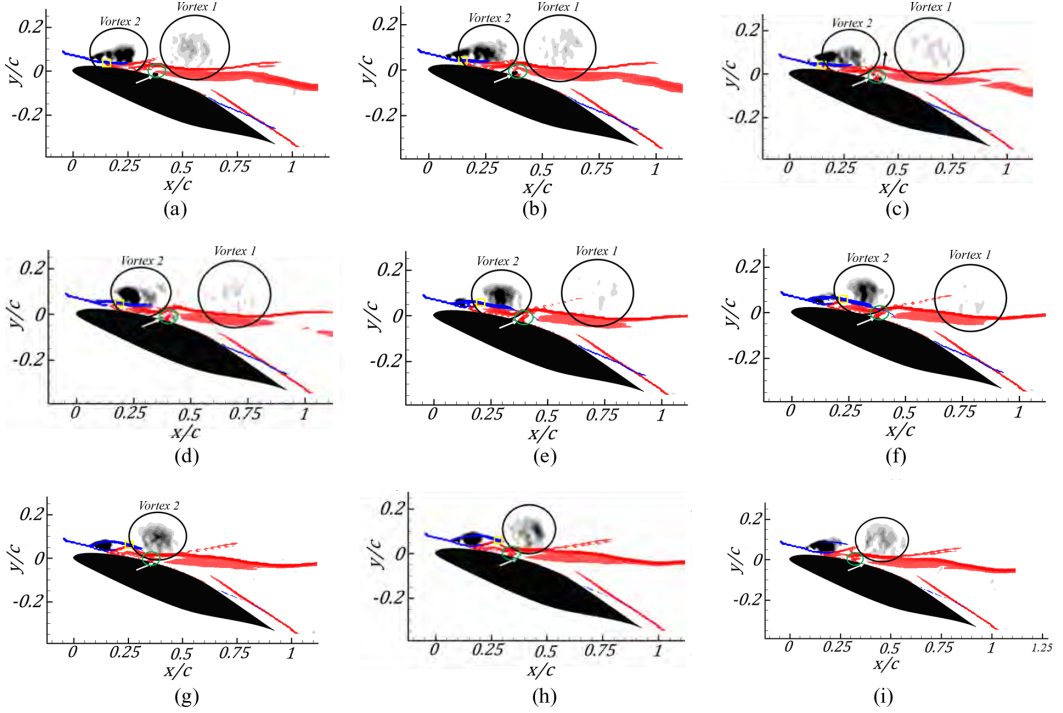


FIG. 9. Contours of phase-averaged Q ($5 < Q^* < 50$), in conjunction with FTLE analysis, at $\alpha = 20^\circ$. Pulse modulation at $f_m^+ \sim O(1)$, SJAs at $x/c = 0.35$, for normalized times of (a) $t_m^* = 0.5$, (b) $t_m^* = 0.6$, (c) $t_m^* = 0.7$, (d) $t_m^* = 0.8$, (e) $t_m^* = 0.9$, (f) $t_m^* = 1.0$, (g) $t_m^* = 1.1$, (h) $t_m^* = 1.2$, (i) $t_m^* = 1.3$.

a vertical line (y -line), and can be expressed as

$$\Gamma_z^* = -\frac{\sum \omega_z^* dx dy}{(m dx dy)} = -\frac{\sum \omega_z^*}{m}, \quad (9)$$

where m is the number of points in the y direction that were used in the calculation. In the case of the SPIV shown here, $m \sim 150$, and in essence, calculates the average vorticity in time along a vertical line. This describes the circulation shed by the airfoil which can be correlated to lift by the unsteady form of the Kutta-Joukowski theorem $L = \rho U_\infty \Gamma + \rho c \frac{\partial \Gamma}{\partial t}$. Figure 10 describes this,

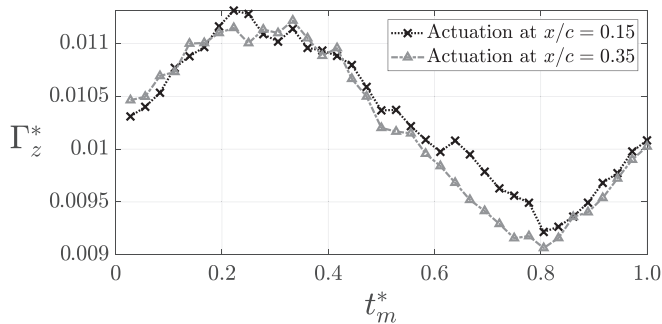


FIG. 10. Variation of the spanwise circulation with time through the trailing edge plane ($x/c = 1.0$) for both actuation locations undergoing pulse modulation at $f_m = 100$ Hz and $DC = 35\%$.

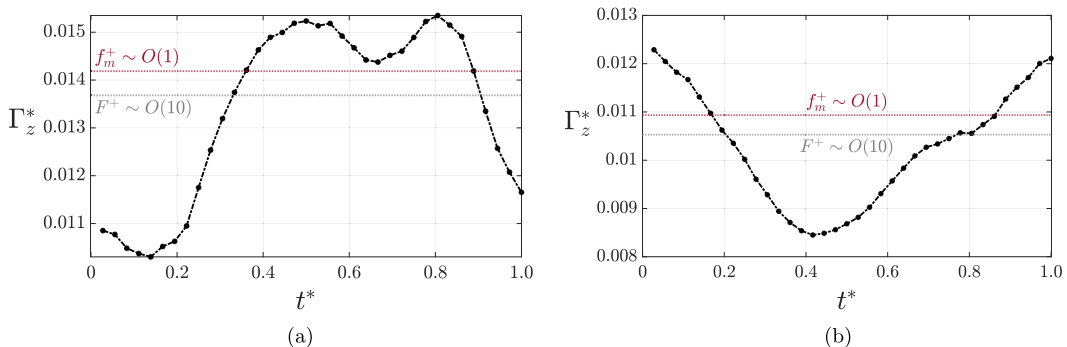


FIG. 11. Variation of the circulation with time calculated at $0.05c$ downstream of the SJA orifice. (a) SJAs at $x/c = 0.15$ and (b) at $x/c = 0.35$. Also included are time-averaged circulation for the continuously actuated [$F^+ \sim O(10)$, gray] and pulse-modulated [$f_m^+ \sim O(1)$, red] cases.

where circulation was calculated through a line at the trailing edge. This was done for both actuation locations. A sinusoidal variation is seen, where it can clearly be observed that circulation is being shed in an unsteady manner from the airfoil, as expected. It is also observed that regardless of actuation location, the change in circulation produced by the actuation is largely unaffected, which can be seen by the relatively similar behavior between the two cases in Fig. 10.

Next, Fig. 11 describes the circulation produced and shed from the SJA when pulse modulated (black) are compared for both SJA locations against the time-averaged circulation produced by a continuously actuated (gray) and pulse-modulated SJA (red) immediately downstream of each respective actuation locations. At both actuation locations, the pulse-modulated case sheds more circulation over the continuously actuated case in the time-averaged sense, and does this with about one third of the power consumption.

A final observation with regard to the benefit of pulse modulation is made in Fig. 12, which in addition more effectively shedding circulation, pulse modulation can also extend the effect of the SJA further in the spanwise direction. This is shown in Fig. 12, where two actuation cases are compared at two spanwise locations. Figures 12(a) and 12(c) are at the *midspan* of the SJA orifice (in agreement with all data presented thus far), and Figs. 12(b) and 12(d) show the flowfield in between jets number 5 and 6. For the continuously actuated case [Fig. 12(a)], red arrows indicate the coherent vortical structures identified by the Q -criterion emanating from the SJA orifice, and the streamlines being altered by the activation of the SJA. However, in between SJAs [Fig. 12(b)], evidence of the SJA is no longer present, as identified by the Q -criterion. On the contrary, when pulse modulation is used, both at the SJA centerline and between jets [Figs. 12(a) and 12(c), respectively], a strong vortical structure is present at both spanwise locations at the same chordwise location. This suggests that perhaps if the SJA spacing is increased, that pulse modulation may have more of a reach in the spanwise direction, reducing (but not eliminating) the dependence on spanwise spacing.

B. Dynamic stall results

This section provides a discussion on the effect of pulse-modulated SJAs on dynamic stall. Sec. III A described how pulse-modulated SJAs can shed circulation more effectively than continuously actuated ones, with the goal of shedding the circulation in a controlled fashion during dynamic stall to control its detrimental effects. To test this hypothesis, shallow dynamic stall is considered first.

1. Shallow dynamic stall

The variation of the lift and pitching moment coefficients during the pulse modulation cycle are presented in Fig. 13. The continuously actuated SJA is shown in grayscale, the pulse-modulated

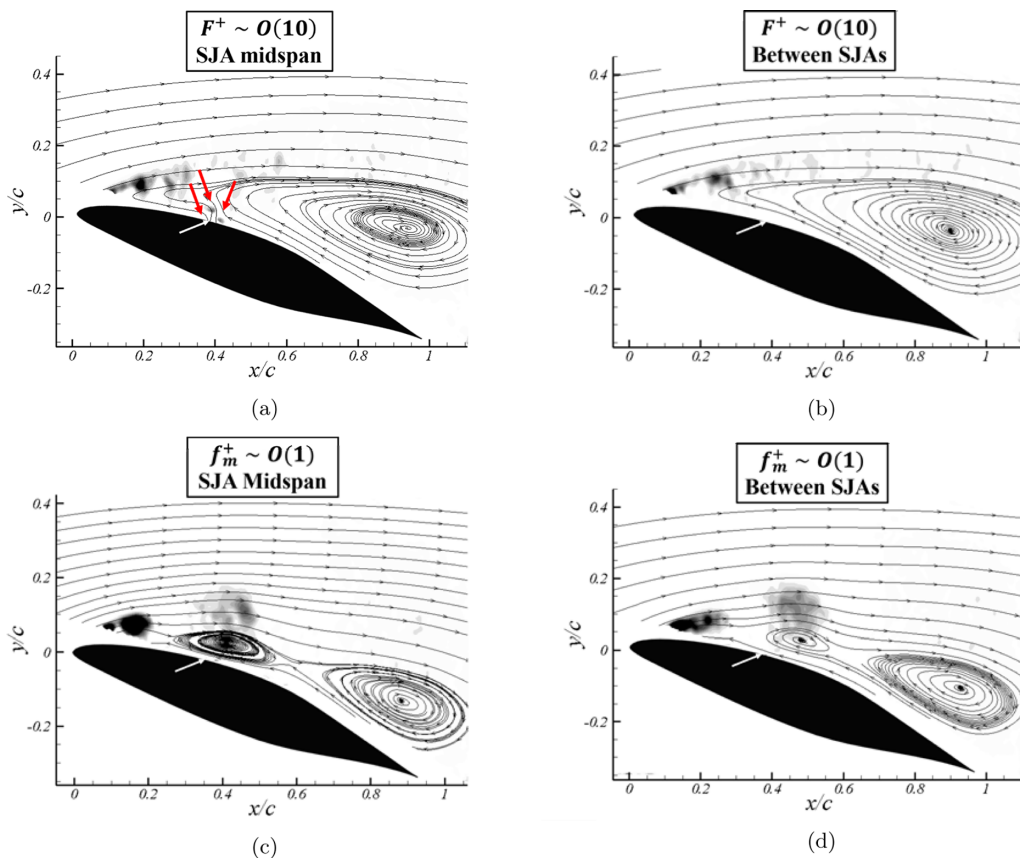


FIG. 12. Contours of phase-averaged Q^* ($5 < Q^* < 50$) with in-plane streamlines when SJAs are at $x/c = 0.35$. (a) The centerline of a continuously actuated SJA, (b) in between two continuously actuated SJAs, (c) the centerline of a pulse-modulated SJA ($f_m = 100$ Hz, $DC = 35\%$), and (d) in-between pulse-modulated SJAs.

case shown in red, and the two are compared to the baseline case shown in black. The baseline case describes commonly observed features of dynamic stall: lift and pitching moment hysteresis and load excursions during stall inception due to the formation and shedding of the dynamic stall vortex (DSV). As can be seen in Fig. 13(a), both actuation techniques reduce the hysteresis, where pulse-modulated SJA further reduce the hysteresis of the load as compared to the continuously actuated case. In fact, the area within the hysteresis curve for the pulse-modulated case is reduced by an additional 63% as compared to the continuously actuated case, which was already reduced 40% from the baseline case. This suggests that the lift coefficient on the upward pitching motion is similar to the lift coefficient on the downward pitching motion. This benefit has the potential of making fatigue modeling more simple and reliable. Moreover, the lift overshoot due to the dynamic stall process is shown to be reduced almost entirely. The lift coefficient as a function of time is shown in Fig. 13(b). The overall profile of the lift coefficient more closely resembles a sine wave, indicating that pulse modulation, at least in the current case presented, has the effect of reducing the detrimental effects of dynamic stall by ensuring a more constant, sinusoidal variation in forcing as compared to the baseline or continuously actuated cases. Also included in Fig. 13(a) is the lift coefficient during static pitch for the actuated cases, where for the pulse-modulated case, the dynamic stall lift coefficient much more closely resembles the static lift coefficient.

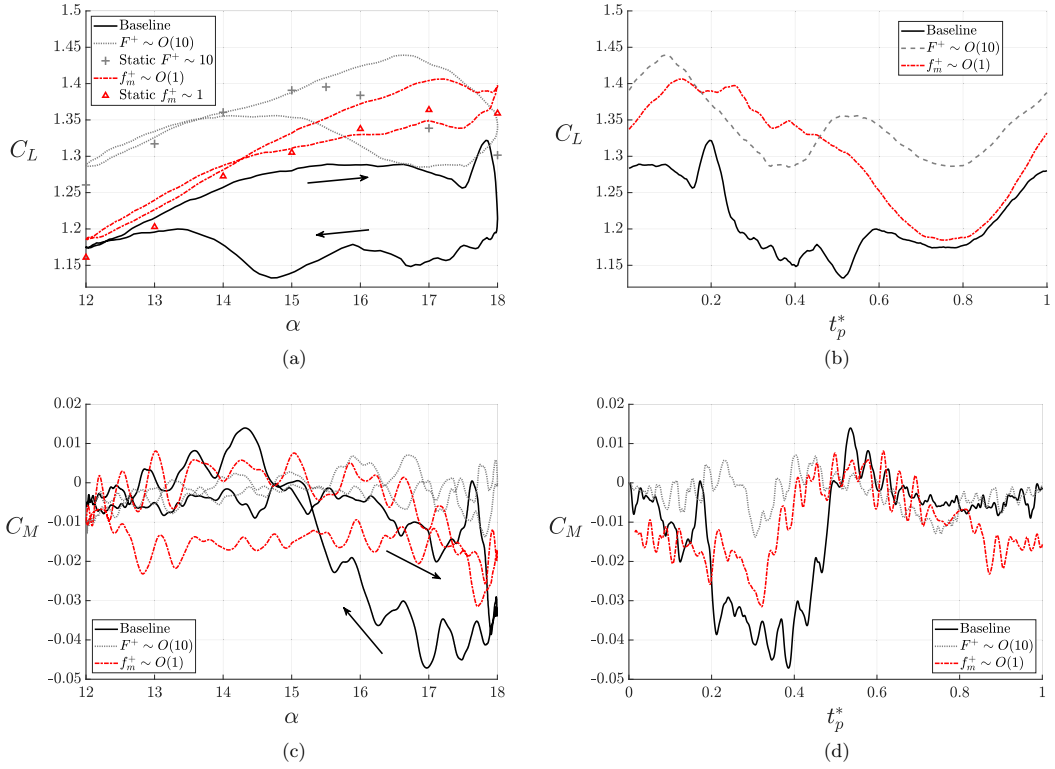


FIG. 13. Control of shallow dynamic stall using continuously actuated and $f_m^+ \sim O(1)$ pulse-modulated SJAs actuated at $x/c = 0.35$. (a, b) Variation of the lift coefficient with angle of attack (with their respective static cases) and time, respectively, and (c, d) pitching moment coefficient variation with angle of attack and time, respectively. The model is pitched at $k_f = 0.025$, $\bar{\alpha} = 15^\circ$, $\alpha_A = 3^\circ$.

Conversely, the pitching moment coefficient exhibits more variation as the airfoil is dynamically pitched, shown in Figs. 13(c) and 13(d). Despite this, the effect of the dynamic stall vortex is largely eliminated (shown in the baseline case at $t^* \sim 0.2$), and the pitching moment coefficient is observed to exhibit less unsteadiness as peak-to-peak variation is reduced as compared to the baseline case. Although not shown for brevity, this is due to the unique phase-averaged pressure distribution along the suction side of the airfoil when pulse modulation is active, and is further investigated in the flowfields shown in Figs. 14 and 15(d). The additional benefits in the pitching moment coefficient could be realized through power consumption, as much of the unsteady loading associated with the DSV is still eliminated, but with only 35% of the power consumed.

Next, the effect of the pulse modulation actuation on the flowfield over the model for shallow dynamic stall is shown in Fig. 14, pitching from $\alpha = 17.1^\circ$ upwards to $\alpha = 18^\circ$ and then downwards to $\alpha = 16.5^\circ$. At $\alpha = 17.1^\circ$ pitching upwards [Fig. 14(a)], the flowfield exhibits typical behavior for this angle of attack: high velocity and attached flow near the leading edge with separation downstream of the three-quarter chord location. Next, at $\alpha = 17.6^\circ$, the boundary layer (upstream of separation) is larger, as observed by the thick, green, contour layer immediately above the actuator surface. This may be suggestive of a separation bubble near the leading edge as has been previously described numerically [39], and is further suggested at $\alpha = 17.9^\circ$ pitching upward [in Fig. 14(c)], where the end of the separation bubble can be observed to be entering the measurement domain directly above the quarter-chord location. This phase-averaged separation bubble drives the hysteresis observed in the pitching moment coefficient when pulse modulation is employed. Regardless, as

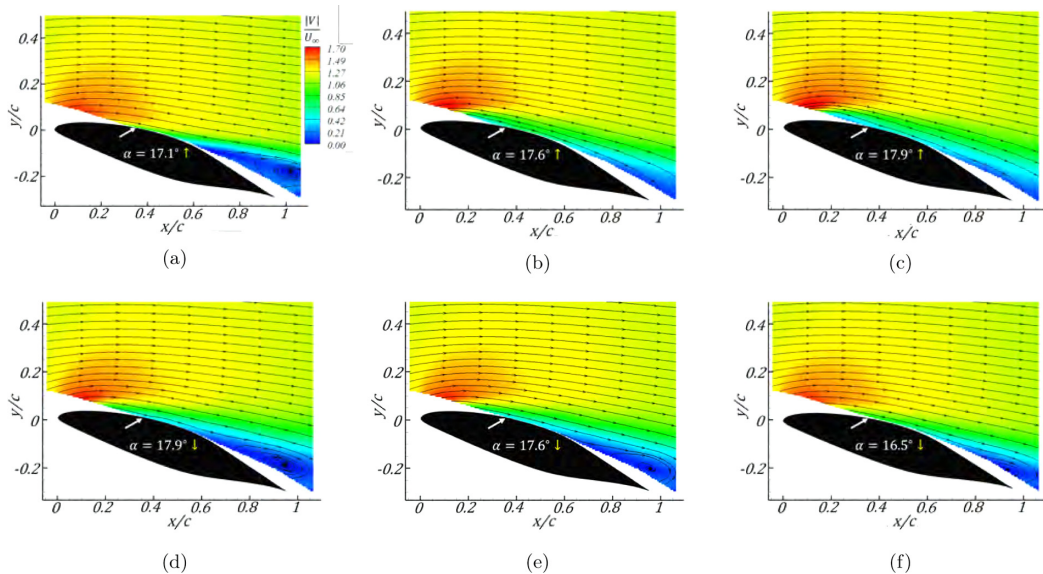


FIG. 14. Phase-averaged normalized total velocity contours, with in-plane streamlines, pitching at $k_f = 0.025$, $\bar{\alpha} = 15^\circ$, and $\alpha_A = 3^\circ$. Angles of attack shown are pitching upward at (a) $\alpha = 17.1^\circ$, (b) $\alpha = 17.6^\circ$, (c) $\alpha = 17.9^\circ$, and pitching downward at (d) $\alpha = 17.9^\circ$, (e) $\alpha = 17.6^\circ$, and (f) $\alpha = 16.5^\circ$. Pulse modulation case with $f_m^+ \sim O(1)$.

can be seen in the flowfields until $\alpha = 16.5^\circ$ pitching downwards [Figs. 14(b)–14(f)], the flowfield remains largely unchanged. The thickness of the boundary layer upstream of the separation location is similar to the upward pitching flowfield, and the trailing edge separation regions size remains relatively constant. This relatively constant size of the leading edge high-velocity region and trailing edge recirculation region is the main driver behind reduced lift hysteresis previously discussed. It should be noted that in these flowfields the pulse modulation is not synchronized to the pitching motion, and thus discrete pulse modulation vortices will not be present. The mechanism of how these vortices develop and shed are investigated in Sec. III A.

A direct comparison of the flowfields when the SJAs were driven with continuous sinusoidal actuation and with pulse modulation during dynamic pitch is shown in Fig. 15. Flowfields are compared at $\alpha = 17.6^\circ$ pitching upwards, and $\alpha = 17.6^\circ$ pitching downward. Comparatively, the pulse-modulated case [Figs. 15(b) and 15(d)] shows a very similar flowfield. These flowfields provide explanation for two of the features of the shallow dynamic stall load profile. First, the lift hysteresis is reduced by preventing drastic changes in the flowfield by reducing the variation of the level of flow separation as direction is changed. Second, the pitching moment coefficient for the pulse-modulated case exhibits larger variation than the continuously actuated case due to the formation of the leading edge phase-averaged separation bubble (which does not occur for the continuously actuated case). Next, an evaluation of the circulation present in the flowfield during shallow dynamic stall is used to further support these observations.

2. Shallow dynamic stall—Circulation evaluation

In this section the variation in circulation observed in the captured SPIV velocity fields is investigated under shallow stall conditions. In order to differentiate the effect that SJAs have on the various flow structures present in the flowfield, the spanwise circulation associated with rotating structures is plotted as a function of normalized pitching time in Fig. 16(a). Here the circulation is normalized by the free-stream velocity and chord length, and the timescale represents the normalized time

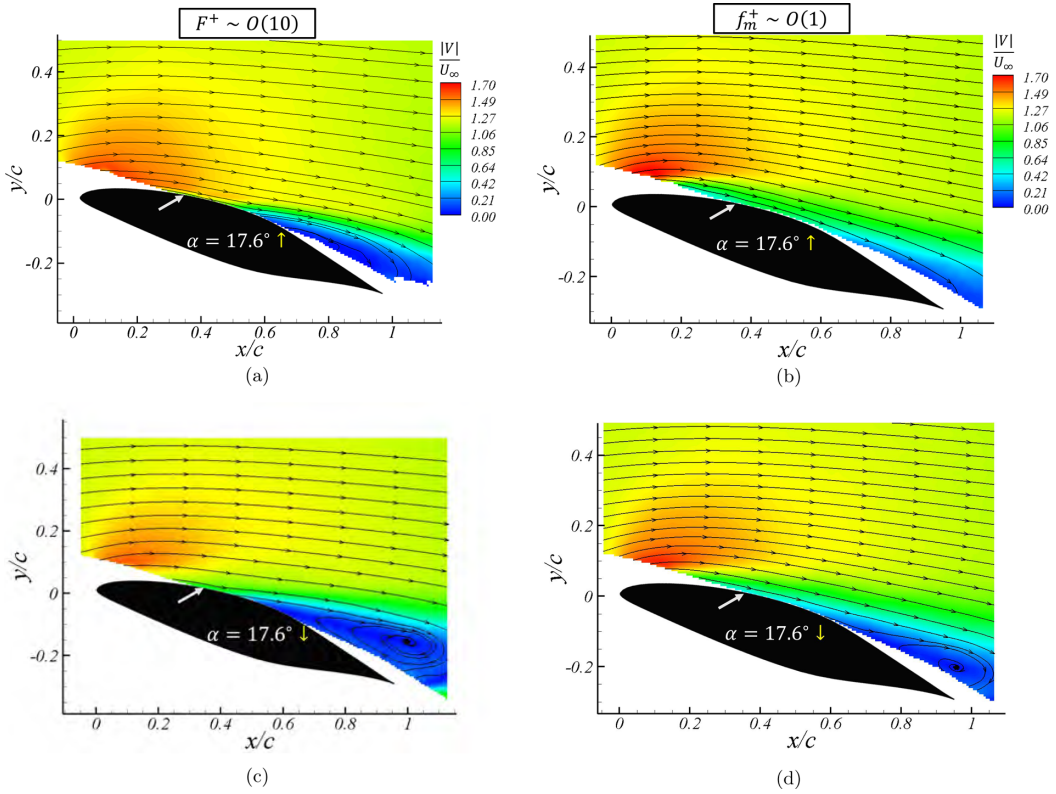


FIG. 15. Color contours of phase-averaged normalized total velocity, with in-plane streamlines, describing dynamic stall inception for the continuously actuated case (left column) and pulse-modulated case (right column). Model pitched at $k_f = 0.025$, $\bar{\alpha} = 15^\circ$, and $\alpha_A = 3^\circ$. Angles of attack shown are (a, b) $\alpha = 17.6^\circ$ upwards and (c, d) $\alpha = 17.6^\circ$ downwards.

of one pitching cycle. The banding of these plots represent the addition and subtraction of the standard deviation of observed circulation based on the variation of the instantaneous PIV frames. A normalized time of zero is at the mean angle of attack, pitching upward during the pitching cycle. For the baseline case [Fig. 16(a)], the circulation pattern exhibited is expected: at higher angles of attack, negative vorticity is concentrated in rotating structures, which is associated with higher circulation and thus higher lift, as was seen in the lift variation (Fig. 13). At lower angles of attack, when the flow can be expected (or observed, in the case of this study) to reattach, the dominant source of vorticity contribution are regions in the flow not associated with rotating structures, likely to be associated with the boundary layer.

Next, SJAs were actuated in order to evaluate how they change the variation of circulation as well as the variation in contribution of circulation, from rotating structures and nonrotating vorticity regions. First, the SJAs were actuated with a sinusoidal waveform at $F^+ \sim O(10)$ [Fig. 16(b)]. The first observation is the notable drop in both the peak total integrated circulation and the integral of circulation on this interval, qualitatively. This result is consistent with prior results demonstrating that the location and trajectory of vortical structures shed during dynamic stall can be altered by the introduction of flow control [22,40]. The effect of pulse-modulated SJAs on the circulation variation was explored and is presented in Fig. 16(c). First, the peak total integrated circulation in the observed velocity field appears to be qualitatively consistent with the total integrated circulation observed in Fig. 16(b), where the jets are actuated at $F^+ \sim O(10)$. However, the difference between

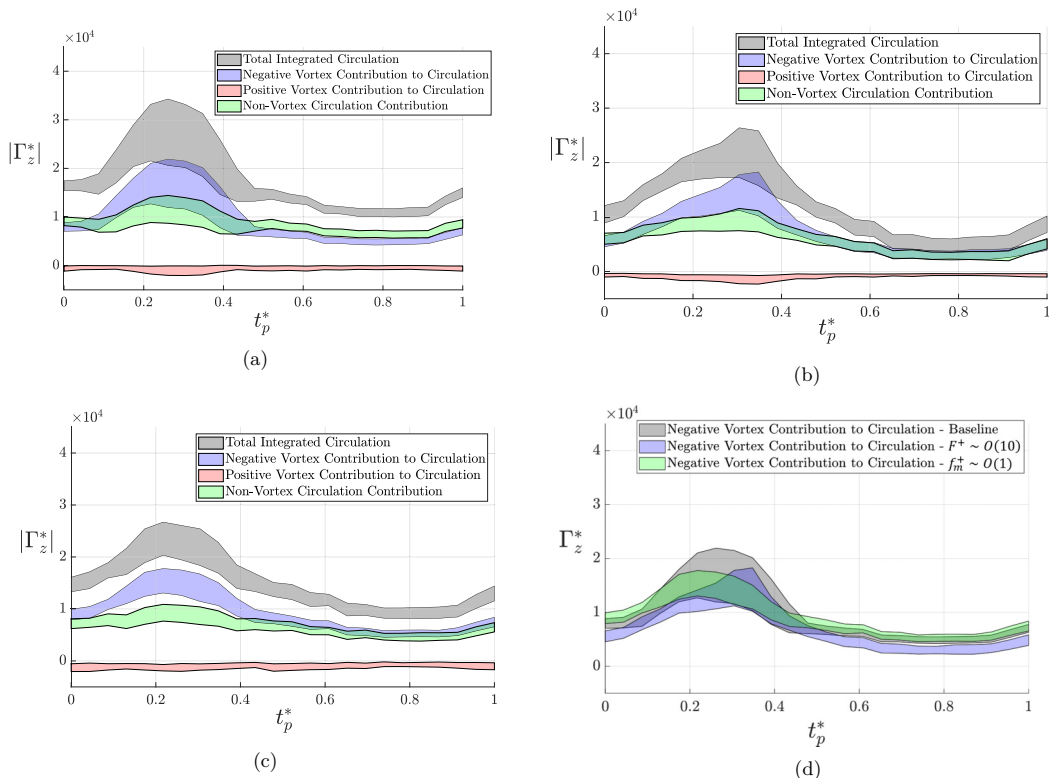


FIG. 16. Variation of the normalized spanwise circulation with normalized time during shallow dynamic stall for (a) the baseline case, (b) continuous actuation with $F^+ \sim O(10)$, (c) pulse modulation actuation at $f_m^+ \sim O(1)$, and (d) a comparison of the negative vortex contribution with varying synthetic jet actuation parameters.

the maximum and minimum circulation is qualitatively less extreme, suggesting that the hysteresis in the lift is smaller, which agrees with the results presented in Fig. 13. Another point of interest, however, occurs at lower angles of attack. The pulse modulation actuation of the jets do not appear to reduce the nonvortex circulation contribution in the same manner that continuous sinusoidal actuation does. This suggests that pulse modulation is acting on the characteristic frequencies associated with the formation and advection of vortical structures without creating such large variations that significant fluctuation in loading occurs.

Figure 16(d) presents a comparison between the two actuation waveforms and the baseline of the variation of the circulation associated with only the negatively rotating structures. Here, in the first half of the cycle, the flowfield is experiencing flow separation, which is where the formation and advection of large scale vortical structures is expected. As can be seen, the actuation of the synthetic jets reduces the strength of these structures, and since these observations are drawn from phase-locked instantaneous data directly, this does not rely on observations of phase-averaged fields to draw a similar conclusion. At the low angles of attack, pulse modulation does not appear to significantly affect the negative vortex contribution to circulation, while continuous actuation has the effect of reducing circulation associated with these negatively rotating structures. This is hypothesized to be due the the circulation being concentrated in the boundary layer instead of shed structures. Finally, it is noted that the variation from frame to frame (the thickness of the bands) is also reduced when utilizing pulse modulation. Pulse modulation results in a smaller variation (both throughout the cycle and from frame-to-frame) in negative vortical structure formation during the

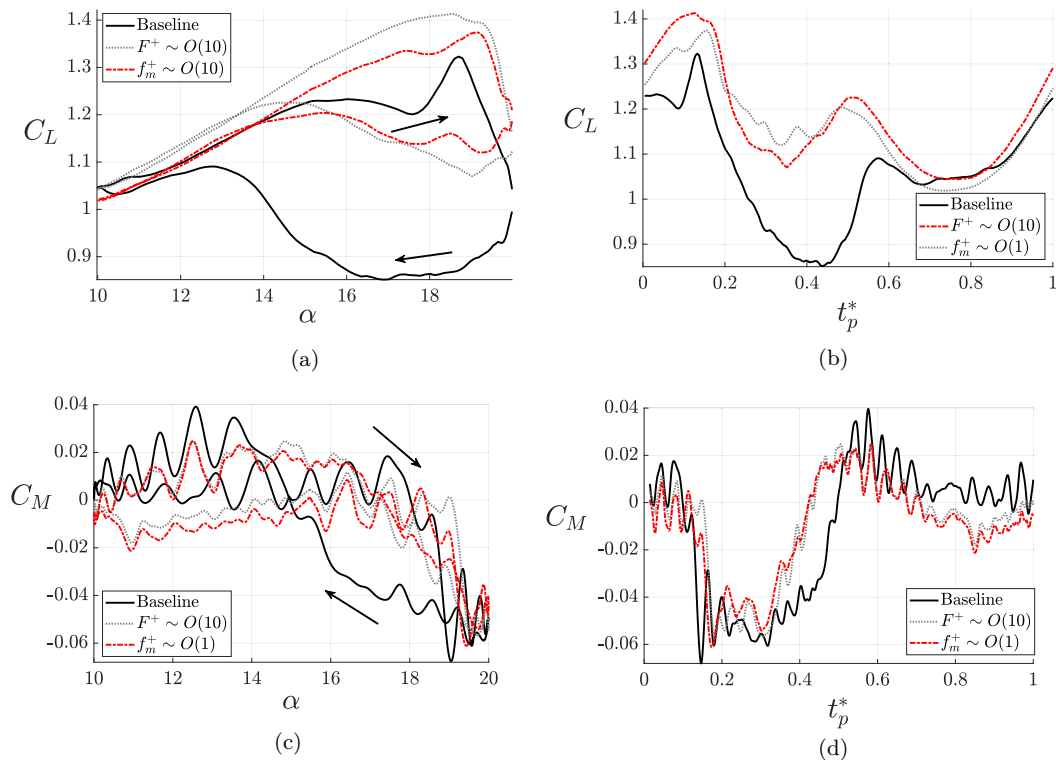


FIG. 17. Control of deep dynamic stall using continuously actuated and pulse-modulated SJAs. Lift coefficient (a) in phase and (b) in time, and pitching moment coefficient (c) in phase and (d) in time. The model is pitched at $k_f = 0.025$, $\bar{\alpha} = 15^\circ$, $\alpha_A = 5^\circ$.

pitching cycle, and this suggests a lower variation and a lower RMS of lift during a dynamic pitch cycle.

3. Deep dynamic stall

The current section performs a similar analysis but on deep dynamic stall, where leading edge flow separation cannot be prevented by the actuation of synthetic jets. The variations of the lift and pitching moment coefficients during deep dynamic stall are shown in Fig. 17. Starting from the lift coefficient [Fig. 17(a)], it is immediately evident that both actuation techniques, once again, reduce the level of hysteresis. More specifically, pulse modulation yields a reduction in the area of the loop as compared to the continuously actuated case, reducing it by 33%. The time trace of lift coefficient, in Fig. 17(b), helps describe the proposed mechanism by which pulse modulation reduces the detrimental effects of deep dynamic stall:

(1) At $t_p^* = 0$ the pulse-modulated and baseline cases have very similar lift coefficient, but as flow separation begins to dominate, the lift is decreased for the baseline case. For the pulse-modulated case, it was shown that lift enhancement is observed when flow separation is more dominant; thus, the lift coefficient continues to increase.

(2) Near $t_p^* = 0.1$, the baseline case begins to undergo dynamic stall, vorticity is gathered near the leading edge as the lift coefficient increases. Lift overshoot occurs, followed by full flow separation as the DSV is shed. Flow separation also occurs for the pulse-modulated case, but as it is continuously shedding vorticity, there is only a dropoff in lift as the flow transitions to fully separated, rather than a large lift overshoot.

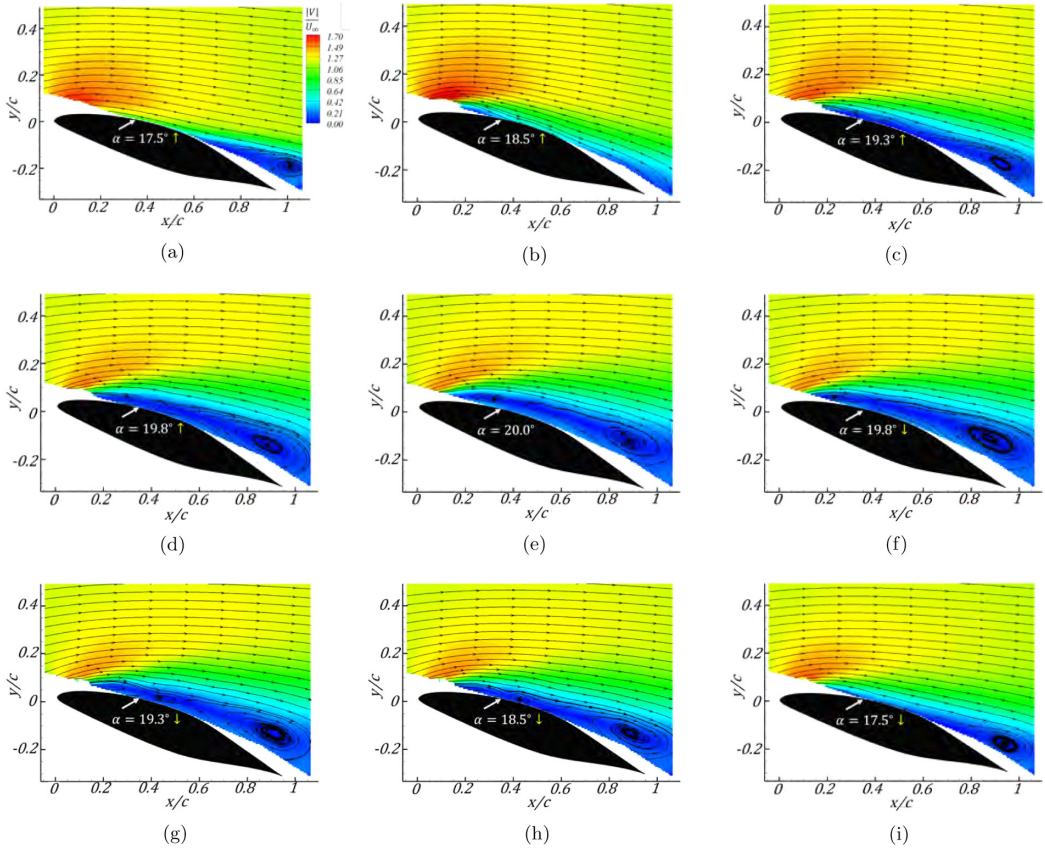


FIG. 18. Phase-averaged normalized total velocity contours with in-plane streamlines describing the pulse-modulated case for the model pitching at $k_f = 0.025$, $\bar{\alpha} = 15^\circ$, and $\alpha_A = 5^\circ$. Angle of attacks shown are pitching upward at (a) $\alpha = 17.5^\circ$, (b) $\alpha = 18.5^\circ$, (c) $\alpha = 19.3^\circ$, (d) $\alpha = 19.8^\circ$, at the top of the cycle at (e) $\alpha = 20^\circ$, and pitching downward at (f) $\alpha = 19.8^\circ$, (g) $\alpha = 19.3^\circ$, (h) $\alpha = 18.5^\circ$, and (i) $\alpha = 17.5^\circ$.

(3) Once the flow is separated, pulse modulation actuation provides lift enhancement over the continuously actuated case by the mechanisms discussed in Sec. III A.

(4) The flow eventually reattaches, near $\alpha = 15^\circ$ pitching downward ($t_p^* = 0.5$), and the pulse-modulated case exhibits lift loads similar to that of the baseline case, and less than the continuously actuated case.

This proposed mechanism describes a critical aspect of flow control. When the flow is attached, control authority is determined by the addition of momentum. This is why a continuously actuated case exhibits higher lift during the upward pitching portions of the cycle, and why continuous actuation shows higher vorticity than pulse modulation in nonrotating regions of the flow. If the flow is dominated by flow separation, control authority is determined by the ability to excite the shed vortical structures within the shear layer, for which pulse modulation appears to be advantageous.

The pitching moment coefficient, presented in Figs. 17(c) and 17(d), shows very similar patterns when the flow is actuated with either continuous sinusoidal waveform or with pulse modulation. Since pitching moment coefficient is dominated by the location of flow separation, the velocity flowfields are analyzed next in Fig. 18. When the airfoil is pitching up at $\alpha = 17.5^\circ$ [Fig. 18(a)] and at $\alpha = 18.5^\circ$ [Fig. 18(b)], the flow is attached. A thick boundary layer is observed at the SJA location as described by the green color contour, and the size of the trailing edge recirculation region is shrunk compared to the baseline case. As the airfoil continues to pitch up to $\alpha = 19.3^\circ$

[Fig. 18(c)], the flow is observed to transition to a fully separated flow. It is this transition to a fully separated flow that causes the pitching moment coefficient to fall to the values shown in Fig. 17(d) at $0.2 < t_p^* < 0.3$. Unfortunately, this deviation in the pitching moment coefficient seems unavoidable, as it is shown to be entirely driven by flow separation.

As the airfoil continues to pitch (from $\alpha = 19.8^\circ$ up to $\alpha = 19.8^\circ$ down), there is very little change in the flowfield. The pulse modulation actuation keeps the separated shear layer relatively close to the airfoil, and the wake is relatively small. Throughout these angles of attack, it is evident that the separated region exhibits two regions of recirculating flow, one near the leading edge, and one downstream of the actuator near the trailing edge. This may suggest that the actuation keeps the trapped vorticity near the leading edge, in the upstream recirculation region. As the airfoil continues to pitch down, the size of the wake (and overall recirculation regions) reduces in size, until reattachment is first seen near the actuator orifice at $\alpha = 17.5^\circ$ pitching downward [Fig. 18(c)], and the flow reattaches as it continues to pitch downward (not shown for brevity).

Compared to the continuously actuated case, a larger beneficial effect can be seen in the flowfields due to pulse modulation. This is shown in Fig. 19, where the velocity fields at three angles of attack during the dynamic pitch process for the continuously actuated case (left) to the pulse-modulated case (right) are compared. It is notable that for the angles of attack shown, the pulse-modulated case shows flowfields that are more similar to each other than the continuously actuated case, which is paramount in reducing the lift hysteresis on the airfoil. Additionally, when the flow is separated for the continuously actuated case, pulse modulation has the ability of pulling the shear layer down towards the airfoil surface, which is how higher lift is achieved. Moreover, it is notable that when pulse modulation is employed in deep dynamic stall, flow separation is evident sooner than with continuous actuation, this is seen at $\alpha = 19.3^\circ$ pitching upward. This is not necessarily undesirable, as flow separation may be bound to occur regardless, and it has been shown that pulse modulation is more beneficial when the flow is separated. Regardless, the pulse-modulated case depicts flowfields whose wakes are notably more consistent over a range of angles of attack, and smaller when the flow is separated, as compared to the continuously actuated case. The next analysis, calculating the vorticity shed by the airfoil, further supports this.

4. Deep dynamic stall—Circulation evaluation

The circulation through the wake during the pitching cycle was calculated for the continuously actuated and the pulse-modulated cases, and is shown in Fig. 20. Here, once again, only the change in negative circulation (i.e., along the suction side of the airfoil) is integrated at $x/c = 1.0$. As can be seen, both the continuously actuated and pulse-modulated cases exhibit an oscillatory behavior, as expected. The change in circulation for the continuously actuated case exhibits a peak smaller than the baseline case, which is why the loads were reduced. Comparing this to the pulse-modulated case, it is evident that the peak of shed circulation, associated with the top of the pitching cycle (near $t_p^* = 0.2$), is notably *smaller* than the continuously actuated case. Moreover, the trough ($0.5 < t_p^* < 1.0$) in the pulse-modulated case is higher than the trough associated with the continuously actuated case. This suggests that pulse modulation allows for a greater shedding of circulation when the flow is attached, and less during the separation process, allowing the variation of the loads during the cycle to be more effectively controlled.

Finally, in order to differentiate the effect that flow control has on the various flow structures present in the flow during deep stall conditions, the variation of the circulation associated with rotating structures, during the normalized pitching cycle is presented in Fig. 21(a). An evaluation of these data would lead to conclusions consistent with previous observations during dynamic stall conditions. At higher angles of attack, where the formation and advection of large scale structures can be anticipated, indeed, the negatively rotating structures are the dominant contribution to circulation increases as compared to the nonvortex circulation contribution. Figure 17 shows the variation in lift during the dynamic pitch cycle. The sharp increase in lift at approximately 10% of normalized time is associated with the formation of a dynamic stall vortex. And indeed, in Fig. 21(a)

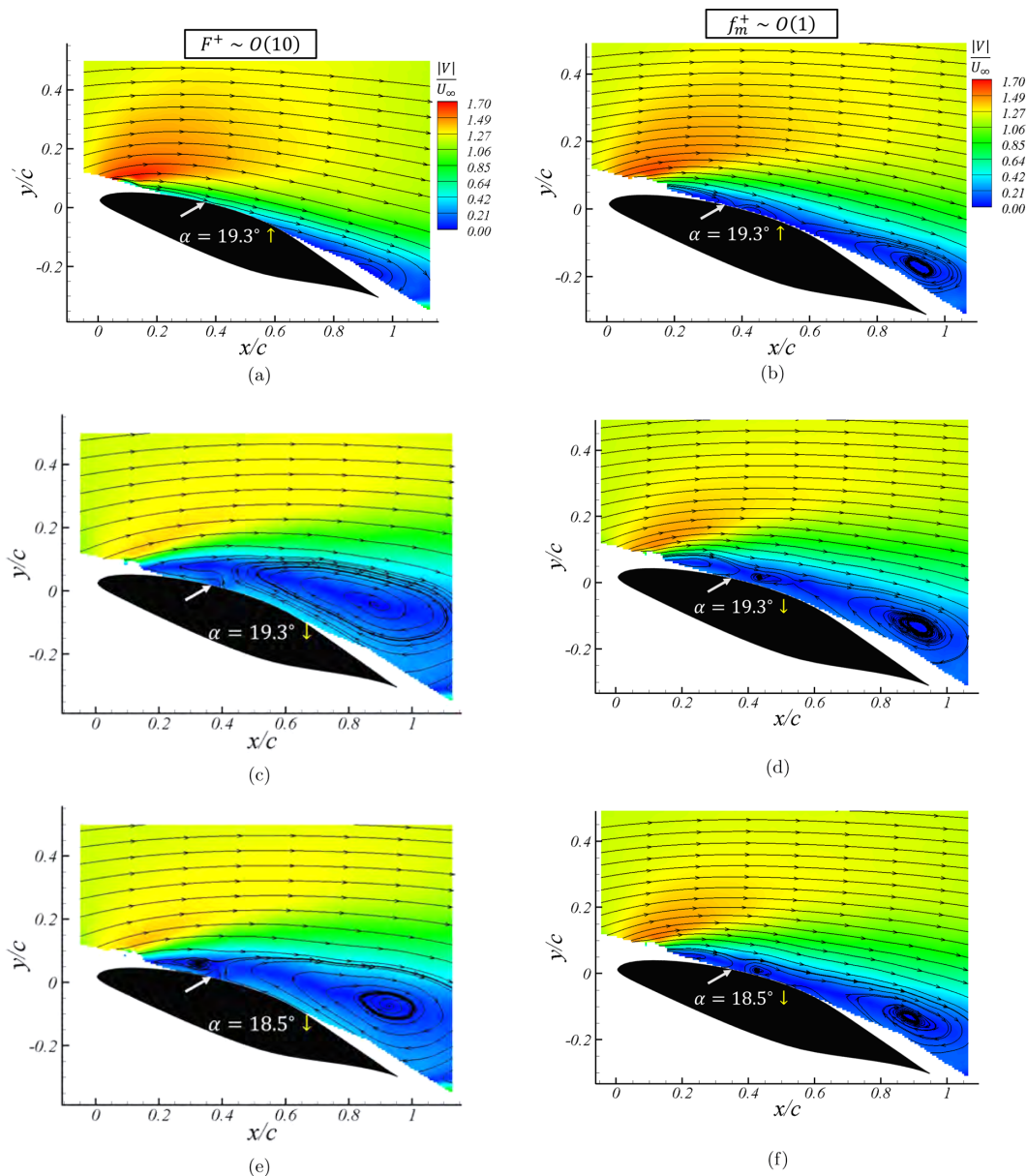


FIG. 19. Phase-averaged normalized total velocity contours, with in-plane streamlines, comparing (a, c, e) continuously actuated case with (b, d, f) pulse-modulated case. Model pitched at $k_f = 0.025$, $\bar{\alpha} = 15^\circ$, and $\alpha_A = 5^\circ$. Angle of attacks shown are (a, b) $\alpha = 19.3^\circ$ pitching upward, (c, d) $\alpha = 19.3^\circ$ pitching downward, and (e, f) $\alpha = 18.5^\circ$ pitching downward.

this is the same time where a large increase in negative vortex contribution to circulation is observed, while the increase in nonvortex circulation contribution is qualitatively appreciably lower.

As was the case for shallow stall, this circulation evaluation was conducted for the continuous actuation. Figure 21(b) shows the variation in circulation contributions from rotating structures and nonrotating regions for the deep dynamic stall conditions, with continuous actuation. Here of note are two apparent phenomena. The time span of relatively high circulation is narrowed, suggesting

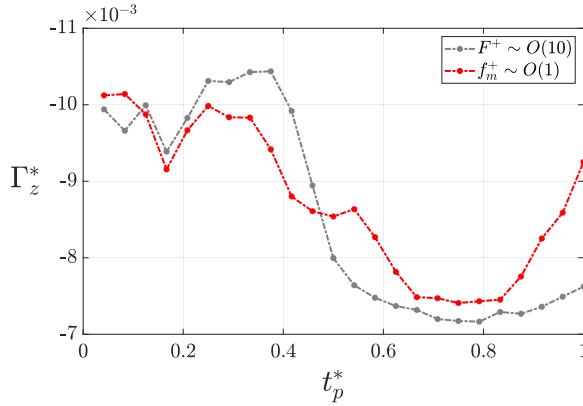


FIG. 20. Change in negative circulation at $x/c = 1.0$ when the model is pitched at $k_f = 0.025$, $\bar{\alpha} = 15^\circ$, and $\alpha_A = 5^\circ$ for the continuously actuated case (gray) and pulse-modulated case (red).

that the duration of separation (in the time-averaged sense) is reduced, or rather that the time period during which formation and advection of large scale structures shed is reduced. Additionally, at lower angles of attack, both negative vortex and nonvortex contributions to circulation are reduced. However, it appears that, at lower angles of attack (or here, the second half of the dynamic pitching

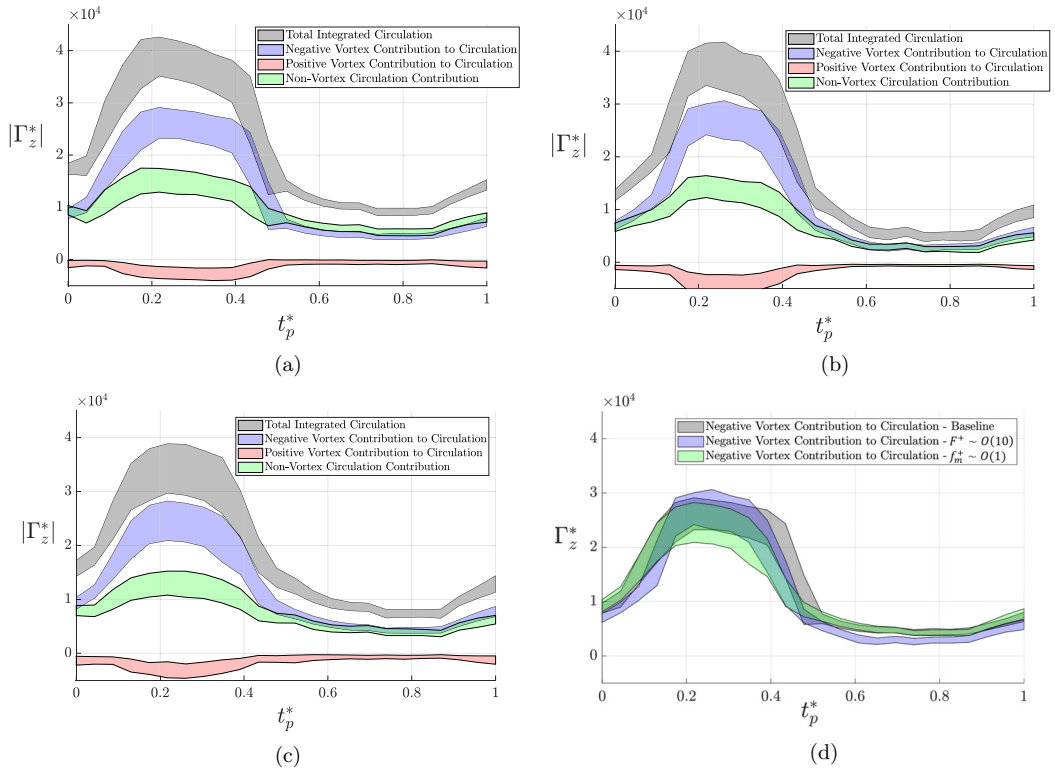


FIG. 21. Normalized circulation with respect to normalized pitching time during deep dynamic stall for (a) the baseline case, (b) continuous actuation case, (c) pulse modulation with $f_m^+ \sim O(1)$, and (d) a comparison of the negative vortex contribution with varying synthetic jet actuation parameters.

cycle), while the circulation observed in negatively rotating structures is lower in the baseline case [Fig. 16(a)], the contribution to circulation from structures and those not identified as structures have settled to the same magnitude. A comparison of this observation to Fig. 17 would suggest that, again, the measurement domain is not large enough to observe all of the circulation needed to find the total lift exerted onto the model. However, this result suggests that at lower angles of attack, actuating the SJAs continuously impacts the boundary layer more than it impacts the formation and advection of large scale negatively rotating structures, as was postulated.

Next, pulse modulation was implemented, and this approach can be evaluated in Fig. 21(c). Here it can be seen that the variation in circulation moving into and out of higher angles of attack (i.e., the first half of the deep dynamic stall pitching cycle) is not as sharp a transition qualitatively as in the case of the continuous actuation case seen in Fig. 21(b). Pulse modulation appears to have the effect of reducing the rate change in variations in circulation as compared to continuous actuation over the full pitching cycle.

Figure 21(d) shows the comparison between the actuation techniques of the circulation measured in negatively rotating structures observed in the flowfield. In this figure, it can be seen that pulse modulation appears to be the most effective at reducing the circulation observed in negatively rotating structures. This would suggest that the reduction in loading, caused by the creation and advection of large scale rotating structures, is due to the disruption of the formation of large-scale structures by the smaller, discrete pulse-modulated structures.

IV. CONCLUSIONS

This work investigated experimentally the hypothesis that the aggressive variations in loads experienced during dynamic stall are directly related to the circulation generated and shed from the airfoil during its pitch cycle. It is suggested that by pulse modulating the synthetic jet actuators at the natural shedding frequency of the separated flow over the airfoil, the shedding of circulation could be controlled and load variation reduced. The Lagrangian observations described the interaction of the various frequencies present in the flow, while the idea that pulse modulation increases shed vorticity with limiting the peak of circulation is corroborated by the Eulerian observations of vorticity present in rotating structures. Several complimentary experiments were conducted to support this overall conclusion. First, the shedding frequency of the airfoil was determined through surface-mounted microphones in its baseline configuration (no actuation). Then the SJAs were pulse modulated at this frequency. It was shown, for the static pitch case, that pulse modulation enhances lift more than a continuously actuated SJA at angles of attack greater than the angle of maximum lift. This suggests that, as expected, a separated shear layer is required in order to manipulate its unstable modes using the pulse modulation technique. The flowfields were first analyzed for the pulse modulation cases in the static sense, and it was shown that regardless of the SJAs' chordwise location, the vortex formation and shedding process was very similar. *Downstream of the SJA, pulse modulation shed more vorticity compared to the continuously actuated method.* It is proposed that the mechanism by which this is achieved is the formation of small vortical structures, which are created at a rate induced by the pulse modulation frequency. This allows a faster amalgamation and advection of vorticity, reducing load variation in contrast to the creation of fewer, larger vortical structures. The Lagrangian coherent structure analysis revealed different mechanisms on how the shed vortex was formed, depending on SJA location. Despite this, the SJAs had a similar impact on the global flowfield.

It was then shown that pulse modulation can improve many aspects of dynamic stall control with synthetic jet actuators, and did so with only 35% of the power consumption compared to continuous actuation. For shallow dynamic stall, the hysteresis in the lift coefficient was dramatically reduced when compared to the continuously actuated case. For deep dynamic stall, similar reduction in lift coefficient hysteresis was also observed, and the mechanism by which the flowfield undergoes dynamic pitching was presented. The proposed mechanism highlighted that when the flow is attached (at low angles of attack), control authority is determined by the addition of momentum

(continuous actuation); whereas when the flow is dominated by flow separation, control authority is determined by the ability to energize the vortical structures within the shear layer. The analysis of the change in circulation through the wake of the airfoil further suggested that pulse modulation can minimize excursions by reducing the vorticity shed from the suction side of the airfoil during stall inception, and increasing the vorticity shed during flow reattachment. Thus, this allows for a greater shedding of circulation during the inception of dynamic stall, allowing less load variation. It is the conclusion of the authors that pulse modulation has a valuable place in the application of synthetic jets to control dynamic stall, and the associated load variations accompanying this phenomenon.

ACKNOWLEDGMENTS

The project was supported by the New York State Energy Research and Development Authority (NYSERDA) and partially by the RPI's Center for Future Energy Systems (CFES).

- [1] M. Amitay, D. R. Smith, V. Kibens, D. E. Parekh, and A. Glezer, Aerodynamic flow control over an unconventional airfoil using synthetic jet actuators, *AIAA J.* **39**, 361 (2001).
- [2] M. Amitay and A. Glezer, Aerodynamic flow control using synthetic jet actuators, in *Control of Fluid Flow*, edited by P. Koumoutsakos and I. Mezic (Springer, Berlin, 2006), pp. 45–73.
- [3] L. N. Cattafesta, III, M. Sheplak, L. N. Cattafesta, and M. Sheplak, Actuators for active flow control, *Annu. Rev. Fluid Mech.* **43**, 247 (2011).
- [4] A. Le Pape, C. Lienard, C. Verbeke, M. Pruvost, and J. De Coninck, Helicopter fuselage drag reduction using active flow control: A comprehensive experimental investigation, *J. Am. Helicopter Soc.* **60**, 1 (2015).
- [5] G. Minelli, E. A. Hartono, V. Chernoray, L. Hjelm, and S. Krajnović, Aerodynamic flow control for a generic truck cabin using synthetic jets, *J. Wind Eng. Ind. Aerodyn.* **168**, 81 (2017).
- [6] D. Velasco, O. López Mejia, and S. Laín, Numerical simulations of active flow control with synthetic jets in a Darrieus turbine, *Renewable Energy* **113**, 129 (2017).
- [7] M. Hatami, F. Bazdidi-Tehrani, A. Abouata, and A. Mohammadi-Ahmar, Investigation of geometry and dimensionless parameters effects on the flow field and heat transfer of impingement synthetic jets, *Int. J. Therm. Sci.* **127**, 41 (2018).
- [8] T. Van Buren, E. Whalen, and M. Amitay, Achieving a high-speed and momentum synthetic jet actuator, *J. Aerosp. Eng.* **29**, 04015040 (2016).
- [9] M. R. Dhanak and B. De Bernardinis, The evolution of an elliptic vortex ring, *J. Fluid Mech.* **109**, 189 (1981).
- [10] C. M. Ho and E. Gutmark, Vortex induction and mass entrainment in a small-aspect-ratio elliptic jet, *J. Fluid Mech.* **179**, 383 (1987).
- [11] B. L. Smith and A. Glezer, The formation and evolution of synthetic jets, *Phys. Fluids* **10**, 2281 (1998).
- [12] C. O'Farrell and J. O. Dabiri, Pinch-off of non-axisymmetric vortex rings, *J. Fluid Mech.* **740**, 61 (2014).
- [13] A. Glezer and M. Amitay, Synthetic jets, *Annu. Rev. Fluid Mech.* **34**, 503 (2002).
- [14] D. Greenblatt and I. J. Wygnanski, Control of flow separation by periodic excitation, *Prog. Aerosp. Sci.* **36**, 487 (2000).
- [15] M. Amitay and A. Glezer, Role of actuation frequency in controlled flow reattachment over a stalled airfoil, *AIAA J.* **40**, 209 (2002).
- [16] A. Glezer, M. Amitay, and A. M. Honohan, Aspects of low- and high-frequency actuation for aerodynamic flow control, *AIAA J.* **43**, 1501 (2005).
- [17] D. Greenblatt and I. J. Wygnanski, Dynamic stall control by periodic excitation, part 1: NACA 0015 parametric study, *J. Aircraft* **38**, 430 (2001).
- [18] D. Greenblatt, B. Nishri, A. Darabi, and I. J. Wygnanski, Dynamic stall control by periodic excitation, part 2: Mechanisms, *J. Aircraft* **38**, 439 (2001).

- [19] H. F. Müller-Vahl, C. Strangfeld, C. N. Nayeri, C. O. Paschereit, and D. Greenblatt, Control of thick airfoil, deep dynamic stall using steady blowing, *AIAA J.* **53**, 277 (2015).
- [20] M. Samimy, N. Webb, and A. Esfahani, Reinventing the wheel: Excitation of flow instabilities for active flow control using plasma actuators, *J. Phys. D: Appl. Phys.* **52**, 354002 (2019).
- [21] M. Amitay and A. Glezer, Controlled, *Int. J. Heat Fluid Flow* **23**, 690 (2002).
- [22] K. Taylor and M. Amitay, Dynamic stall process on a finite span model and its control via synthetic jet actuators, *Phys. Fluids* **27**, 077104 (2015).
- [23] J. C. R. Hunt, A. A. Wray, and P. Moin, Eddies, streams, and convergence zones in turbulent flows, in *Center for Turbulence Research, Proceedings of the Summer Program 1988* (Stanford University, CA, 1988), pp. 193–208.
- [24] J. Jeong and F. Hussain, On the Identification of a Vortex, *J. Fluid Mech.* **285**, 69 (1995).
- [25] M. S. Chong, A. E. Perry, and B. J. Cantwell, A general classification of three-dimensional flow fields, *Phys. Fluids* **2**, 765 (1990).
- [26] L. Graftieux, M. Michard, and N. Grosjean, Combining PIV, POD and vortex identification algorithms for the study of unsteady turbulent swirling flows, *Meas. Sci. Technol.* **12**, 1422 (2001).
- [27] G. Haller, An objective definition of a vortex, *J. Fluid Mech.* **525**, 1 (2005).
- [28] G. Haller and G. Yuan, Lagrangian coherent structures and mixing in two-dimensional turbulence, *Physica D* **147**, 352 (2000).
- [29] G. Haller, Lagrangian coherent structures from approximate velocity data, *Phys. Fluids* **14**, 1851 (2002).
- [30] Y. Huang and M. A. Green, Detection and tracking of vortex phenomena using Lagrangian coherent structures, *Exp. Fluids* **56**, 147 (2015).
- [31] M. A. Green, C. W. Rowley, and A. J. Smits, The unsteady three-dimensional wake produced by a trapezoidal pitching panel, *J. Fluid Mech.* **685**, 117 (2011).
- [32] W. J. McCroskey, The phenomenon of dynamic stall, NASA technical memo 81264 (1981), <https://ntrs.nasa.gov/api/citations/19810011501/downloads/19810011501.pdf>.
- [33] W. J. McCroskey, Unsteady airfoils, *Annu. Rev. Fluid Mech.* **14**, 285 (1982).
- [34] T. Rice, In-depth study of dynamic stall control: Fundamentals to application, Ph.D. thesis, Rensselaer Polytechnic Institute, 2019.
- [35] T. Van Buren, M. Beyar, C. M. Leong, and M. Amitay, Three-dimensional interaction of a finite-span synthetic jet in a crossflow, *Phys. Fluids* **28**, 037105 (2016).
- [36] T. T. Rice, K. Taylor, and M. Amitay, Wind tunnel quantification of dynamic stall on an S817 airfoil and its control using synthetic jet actuators, *Wind Energy* **22**, 21 (2018).
- [37] A. Sciacchitano and B. Wieneke, PIV uncertainty propagation, *Meas. Sci. Technol.* **27**, 084006 (2016).
- [38] LCS MATLAB Kit v2.3, <http://dabirilab.com/software>.
- [39] M. R. Visbal and D. J. Garmann, Analysis of dynamic stall on a pitching airfoil using high-fidelity large-eddy simulations, *AIAA J.* **56**, 46 (2018).
- [40] K. Taylor, C. M. Leong, and M. Amitay, Load control on a dynamically pitching finite span wind turbine blade using synthetic jets, *Wind Energy* **18**, 1759 (2015).